FEDERAL UNIVERSITY OF TECHNOLOGY – PARANÁ

OFFICE OF RESEARCH AND GRADUATE STUDIES

GRADUATE PROGRAM IN MECHANICAL ENGINEERING

ADRIANO KOSSOSKI

THERMAL CONTROL OF A SHAPE MEMORY ALLOY FOR ACTUATION IN THE SOMMERFELD EFFECT OF A NON-IDEAL SYSTEM

MASTER'S THESIS

PONTA GROSSA

2018

ADRIANO KOSSOSKI

THERMAL CONTROL OF A SHAPE MEMORY ALLOY FOR ACTUATION IN THE SOMMERFELD EFFECT OF A NON-IDEAL SYSTEM

Master's Thesis presented as a partial requirement for obtaining a Master's Degree in Mechanical Engineering from the Graduate Program in Mechanical Engineering, Federal University of Technology – Paraná.

Advisor: Prof. Dr. Angelo Marcelo Tusset
Co-Advisor: Prof. Dr. Gerson Henrique dos Santos

PONTA GROSSA

2018

FOLHA DE APROVAÇÃO

Título de Dissertação Nº **20/2018**

THERMAL CONTROL OF A SHAPE MEMORY ALLOY FOR ACTUATION IN THE SOMMERFELD EFFECT OF A NON-IDEAL SYSTEM

Por

Adriano Kossoski

Esta dissertação foi apresentada às **8 horas** de **11 de junho de 2018** como requisito parcial para a obtenção do título de MESTRE EM ENGENHARIA MECÂNICA, com Área de Concentração em Térmica e Fluidos, Programa de Pós-Graduação em Engenharia Mecânica. O candidato foi arguido pela Banca Examinadora, composta pelos professores abaixo assinados. Após deliberação, a Banca Examinadora considerou o trabalho **APROVADO**.

_____
Prof. Dr. Airton Nabarrete (ITA)

_____
Prof. Dr. José Manoel Balthazar (UTFPR)

_____
Prof. Dr. Vinícius Piccirillo (UTFPR)

_____
Prof. Dr. Angelo Marcelo Tusset (UTFPR)
Orientador e Presidente da Banca

Visto do Coordenador:

_____
Prof. Dr. Anderson Geraldo Marenda
Pukasiewicz
Coordenador do PPGEM
UTFPR – Câmpus Ponta Grossa

- A Folha de Aprovação assinada encontra-se arquivada na Secretaria Acadêmica -

ACKNOWLEDGMENTS

RESUMO

Os estudos da vibração mecânica e do comportamento de um sistema dinâmico se caracterizam como atividades essenciais em projetos de engenharia. Além da vibração mecânica, sistemas eletromecânicos podem apresentar outro tipo de comportamento, onde ocorre a troca de energia entre a estrutura mecânica e a(s) fonte(s) de excitação. Estes sistemas recebem a classificação de sistemas não ideias. Neste tipo de sistema, ao mesmo tempo em que a fonte de alimentação influencia diretamente a dinâmica da estrutura mecânica, a fonte de excitação sofre uma influência recíproca da estrutura, alterando seu comportamento e causando uma perda de energia que seria utilizada pelo(s) motor(es). Surge então o interesse da aplicação de materiais inteligentes para a atenuação e controle dos efeitos que surgem neste tipo de sistema. Os materiais inteligentes possuem a capacidade de alterar alguma propriedade específica na presença de determinado impulso, alterando características físicas quando necessário e assim, podendo servir como sensores e/ou atuadores. Esta dissertação de mestrado contribui para área do estudo dos materiais inteligentes, propondo uma abordagem de controle da vibração e do efeito Sommerfeld em um sistema não ideal através do uso de um atuador do tipo Liga com Memória de Forma (LMF) – material que possui a capacidade de alterar sua forma física em presença de uma alteração de temperatura. Inicialmente, é feita a caracterização de um atuador LMF através de um experimento prático, onde diversas tensões elétricas são aplicadas sobre o material. Estas tensões são posteriormente relacionadas com a recuperação da deformação, corrente elétrica consumida e com as temperaturas de superfície do atuador. Onde para a obtenção das temperaturas do material LMF foram utilizados sensores de fibra ótica, específicos para esta aplicação. Para demonstrar a funcionalidade do atuador com memória de forma, um protótipo equivalente do sistema do tipo não ideal foi construído e instrumentado. Após o sistema ter seu comportamento avaliado, foi proposto a instalação de um atuador LMF sendo o mesmo ativado através de um controlador ON/OFF projetado.

Palavras-chave: Vibração. Dispositivos eletromecânicos. Controle de temperatura. Engenharia mecânica.

ABSTRACT

KOSSOSKI, Adriano. **Thermal Control of a Shape Memory Alloy for Actuation in the Sommerfeld Effect of a Non-Ideal System**. 2018. 94 p. Master's Thesis (Master's Degree in Mechanical Engineering) - Federal University of Technology - Paraná. Ponta Grossa, 2018.

The studies of mechanical vibration and the behavior of a dynamic system are characterized as essential activities in engineering projects. In addition to the mechanical vibration, electromechanical systems can present another type of behavior, where occur an energy exchange between the mechanical structure and the source(s) of excitation. These systems are classified as non-system systems. In this type of system, at the same time that the power supply directly influences the dynamics of the mechanical structure, the excitation source suffers a reciprocal influence, altering his behavior and causing a loss of energy that would be used by the motor(s). Nowadays, the interest in the use of the so-called smart materials for the attenuation and control of the effects that can appear in these complexes systems are increasing. The smart materials have the ability to change some specific property in the presence of a certain impulse, changing physical characteristics when necessary and thus, being able to serve as sensors and/or actuators. This master's thesis contributes to the study of the smart materials area proposing the control of the vibration and Sommerfeld effect in a non-ideal system through the use of a Shape Memory Alloy (SMA) actuator - material that has the ability to change the physical form when undergoing a change in his temperature. Initially, the characterization of the SMA actuator is done through a practical experiment, where several electric voltages are applied to the material. These voltages are subsequently related to the physical recovery, electric current consumed and to the surface temperatures of the actuator. To obtain the temperatures of the SMA material were used Fiber Bragg Grating (FBG) sensors, specific for this application. To demonstrate the functionality of the shape memory actuator, an equivalent prototype of the non-ideal type system was constructed and instrumented. After analyzing the behavior of the system, it was proposed the installation of an SMA actuator that will be activated through a projected ON/OFF controller.

Keywords: Vibration. Electromechanical devices. Temperature control. Mechanical engineering.

LIST OF FIGURES

LIST OF TABLES

LIST OF INITIALISMS AND ACRONYMS

LIST OF INITIALISMS

AC	Alternating Current
CEMF	Counter-electromotive Force
DC	Direct Current
FBG	Fiber Bragg Grating
FFT	Fast Fourier Transform
LPF	Low Pass Filter
ODE	Ordinary Differential Equation
SMA	Shape Memory Alloy
SME	Shape Memory Effect
SMM	Shape Memory Material
PWM	Pulse Width Modulation

LIST OF ACRONYMS

CAE	Computer-Aided Engineering
FEM	Finite Element Method
DAQ	Data Acquisition

LIST OF SYMBOLS

Greek Symbols	Quantity	Units
Ω	Phase transformation modulus	GPa
ε	Strain	mm/mm
Θ	Thermoelastic modulus	$MPa/^{\circ}C$
π	Pi	-
φ	Displacement of the shaft	rad
ξ	Martensitic volumetric fraction	-
ρ	Density	kg/m^3
σ	Mechanical stress	MPa
ω	Frequency	Hz

Latin Symbols	Quantity	Units
A	Area	m^2
A_f	Austenite finish temperature	$^{\circ}C$
A_s	Austenite start temperature	$^{\circ}C$
c_p	Specific heat	$J/(kg.K)$
d	Diameter	m
E	Young's modulus	GPa
E_k	Kinetic energy of a dynamical system	J
E_p	Potential energy of a dynamical system	J
f	Frequency	Hz
g	Gravitational acceleration	m/s^2
h	Runje-Kutta algorithm step size	-
h_C	Convective heat transfer coefficient	$W/(m^2.^{\circ}C)$
I	Electric current	A
K_B	Counter-electromotive force constant	$N.m/A$
K_T	Torque constant.	$V.s/rad$
L	Inductance	H

L_g	Lagrangian function	-
l	Length	m
m	Unbalanced mass	kg
M	Total mass from the non-ideal system	kg
M_f	Martensite finish temperature	$^{\circ}C$
M_s	Martensite start temperature	$^{\circ}C$
R	Electric resistance	Ω
T	Temperature	$^{\circ}C$
T_q	Torque generated	$N.m$
V	Electric voltage	V
V_{CEMF}	Counter-electromotive Force	V

Subindex

A	Austenite
act	Actuator
cr	Critical
M	Martensite
mtr	Motor
sf	Surface
o	Initial
∞	Ambient
n	Natural
S	Stress-induced/related
T	Temperature-induced/related

CONTENTS

1 INTRODUCTION

This chapter presents the foundations of this master's thesis. Initially, an introduction to the main themes of this thesis will be presented, with a focus on the non-ideal systems and the use of the shape memory alloys actuators. In the sequence, the motivations and objectives are described, ending the chapter with a summary of the thesis structure.

1.1 THE NON-IDEAL SYSTEMS AND THE USE OF THE SMART MATERIALS

Nowadays, with the evolution of technology has emerged a growing demand for more lightweight and larger electromechanical systems. These configurations are present in several systems and projects, such as robotic manipulators, portal frame systems and the most diverse structures that are subject to some type of slewing movements (e. g., satellite panels, space antennas, and flexible cranes). However, these more flexible electromechanical structures are susceptible to specific mechanical vibrations phenomena. The union between the mechanical structure and the rotational energy source causes a specific behavior in the system, i.e., an energy exchange between the mechanical system and the rotational/electric system. Because of this specific behavior, this kind of system received a new classification with the name of non-ideal systems (BALTHAZAR et al., 2003, 2004; PICCIRILLO; TUSSET; BALTHAZAR, 2014).

In the non-ideal systems, the energy source, usually a DC motor due to the ease of implementation and speed control, which is responsible for exciting the system, undergoes a reciprocal influence, altering its own performance. This effect becomes very perceptible when the system passes through the resonance region of the structure, where it is possible to observe increases in vibration amplitudes and loss of motor rotation energy.

One of the options proposed by some research to attenuate the non-ideal behavior is the coupling of the system with some type of actuator. This option is generally chosen because the use of an external actuator avoids changes in the mechanical design or concept, often unviable in some projects. For the actuators, arises the interest to use the so-called smart materials. This special type of material

has some kind of active response to a specific impulse. As they are often simple in constitution, they have ease of merging with the dynamic system (LAGOUDAS, 2008; MAVROIDIS, 2002; PICCIRILLO; TUSSET; BALTHAZAR, 2014).

The materials that are part of this special group have some specific characteristics that allow them to change their physical or chemical structure through certain external impulses. The impulse for activation depends on the type of material and can be of the most varied types, such as an electric voltage, a magnetic field, a change in temperature, etc. Because of this special behavior, these materials can be used as sensors and/or actuators. Among these materials are ceramics, polymers and large variations of metallic alloys (LAGOUDAS, 2008; LEO, 2007).

There is a vast amount of materials in this classification, and consequently, there are several types of effects that these materials may present. A specific kind of material widely used as actuators are the materials with Shape Memory Effect (SME). Basically, after suffering a type of plastic deformation, this type of material can return to its original/memorized form through a heating process. Another characteristic of these materials is the superelasticity, where above a certain temperature, after being deformed through a mechanical loading, these materials tend to return to their original form after the loading is removed. The most known material that has these two effects are the Shape Memory Alloys (SMA) (LAGOUDAS, 2008; LEO, 2007).

The shape memory effect was first observed in a gold-cadmium (*AuCd*) alloy by Arne Ölander in 1932. It was observed that this material had a structural return after undergoing an increase of their thermal energy (SME). But it was only after the results using a Nickel-Titanium (*NiTi*) alloy presented by the Naval Ordnance Laboratory (USA) in 1961, that this effect awakened interest for engineering projects. This new alloy, which received the trade name *Nitinol,* demonstrated easier use when compared to other materials, also showing other positive characteristics, such as high biocompatibility, excellent corrosion resistance, great physical recovery, etc.

With renewed interest in these new metal alloys, several studies and projects began to be made. Due to the aforementioned characteristics of biocompatibility and great elastic strain range, several biomedical projects have created, such as stents, inferior vena cava filters, medical instruments, and material for orthodontics (MACHADO; SAVI, 2003). The capacity to absorb energy was studied in areas of vibration control, where absorbers and devices in various formats have emerged

(SAADAT et al., 2002). The shape memory effect also was the object of research in several actuator designs, and because of its ability to perform work, this kind of material has been used both to replace conventional actuators and to create entirely new types.

1.2 MOTIVATIONS

The demand for lighter, larger dimensions and flexible electromechanical structures it is turning a very common practice in engineering design. However, these systems were also more susceptible to the common mechanical vibration and some special type of vibration, i.e., non-ideal type. In this kind of system, there is a behavioral relationship between the electrical and the mechanical subsystems. Where depending on the frequency of operation, energy losses may occur, and the rising of harmful vibration frequencies can appear in the system.

Since Sommerfeld's discovery in 1902 of the first effect considered non-ideal, some important research on the subject was done. However, for Balthazar et al. (2003), when compared to the ideal systems, still few works in the literature are dedicated to non-ideal type systems. As the effects that arise in non-ideal systems are usually unwanted mechanical vibrations, the attenuation or control of non-ideal behavior is a goal to achieve.

Materials classified as smart are a great option for such cases, since these materials, besides being used as part of the mechanical structure like a common material, can act directly on the behavior of the system and can be used as active, passive or semi-active control actuators.

1.3 RESEARCH OBJECTIVES

The main objective of this master's thesis is stated as follows: *to attenuate and control the Sommerfeld effect in a non-ideal type system using semi-active shape memory alloy actuators*.

The specific objectives defined for this purpose are:

1. Review the fundamental concepts of shape memory alloys, with emphasis on the most common mathematical models (Chapter 2);

2. Experimentally observe and characterize an SMA actuator to obtain its constituent parameters needed for a phenomenological model (Chapter 3);

3. Develop a mathematical model that represents the coupling between the mechanical and the electrical system of a non-ideal system (Chapter 4);

4. Build a real system and implement the SMA actuator (Chapter 5).

1.4 METHODOLOGY AND THESIS ORGANIZATION

This master's thesis focuses on the implementation of a shape memory alloy actuator to attenuate the Sommerfeld effect and the vibration of a non-ideal system. The methodology used can be divided into two: a theoretical approach for the non-ideal system and an experimental approach for the non-ideal system and SMA actuator.

For the theoretical part of this master's thesis, numerical procedures and simulations were developed. The already existing phenomenological models of SMA were studied and implemented, with an emphasis in the Elahinia's model. Was also described the modeling of a non-ideal type system composed of a cantilever beam and an electric DC motor. The final numerical results presented in this thesis already take into account the parameters of the mechanical and electrical system obtained experimentally.

In the experimental part of this thesis, a non-ideal system was built for testing. Initially, all the physical parameters of this system are obtained. The behavior of the system in operation is studied. It is proposed to use an SMA actuator to attenuate the characteristic vibration effect of this type of system.

This file is divided into six (6) main chapters and three (3) appendixes. Chapter 2 presents the basic concepts about shape memory alloys, their characteristic effects, and behavior. In addition, its advantages and disadvantages are also presented, as well as its main phenomenological mathematical models.

Chapter 3 presents an experimental study of the behavior of an SMA actuator implemented in a specific system. This chapter has the objective to show the basic operation of an SMA actuator, showing his behavior in the heating and cooling process. This analysis will be used to understand the SMA functionality and implementation.

Chapter 4 is concerned with the presentation of the mathematical model of the non-ideal system and the numerical simulations of this model. A Mathematical Runje-Kutta integrator is described, where the constructed algorithm was used to simulate the non-ideal system. All the simulations carried in this chapter uses parameters obtained experimentally from a real non-ideal system.

Chapter 5 presents the construction of the non-ideal system object of study from this thesis and the proposed control of the Sommerfeld effect using shape memory alloy actuators. The prototype of the non-ideal system and his instrumentation are described. In the sequence, the proposed control of the Sommerfeld effect is defined, presenting the results for the system with and without the SMA actuator.

Chapter 6 presents the conclusions, contributions and future works related to this thesis.

2 FUNDAMENTALS AND APPLICATION OF SHAPE MEMORY ALLOYS

This chapter aims to present the main concepts and fundamentals of Shape Memory Alloys (SMA). The chapter begins with the basic theory of SMA with emphasis on the two main characteristic effects of this type of material: the Shape Memory Effect (SME) and the superelasticity. In the following, are presented advantages and disadvantages in the use of this kind of material. The chapter concludes with a presentation of the most well-known phenomenological mathematical models developed for the SMA materials.

2.1 SMART MATERIALS AND THE SHAPE MEMORY ALLOYS

Over the time, several studies of materials that present different characteristics and behaviors have emerged, special materials that demonstrate a certain response when in contact with some specific excitation. These materials were classified into a new group and received the title of smart materials. When in the presence of a specific excitation, this kind of material can change some physical and structural characteristics, generating forces, and changing the environment where they are. The excitation mentioned depends on the type and class of material and can be an electrical voltage, a magnetic field, a mechanical stress, a change in the temperature, etc (LAGOUDAS, 2008; LEO, 2007).

Among these materials, are highlighted those who can change and maintain their physical form through a specific stimulus, these are the so-called Shape Memory Materials (SMM). In this class of materials, a certain physical form of the system can be maintained indefinitely until an external stimulus is performed. Due to this function, this type of material has found a wide range of applications in several areas of engineering. The Shape Memory Alloys (SMA) are part of the SMM class and have the ability to recover a certain physical form when the system temperature is increased. This return to a previous form can occur even if the system is under mechanical loading, thus representing a capacity of work.

Various metallic alloys can exhibit shape memory effect and superelasticity. According to Sun et al. (2012), SMA materials can be divided into three groups according to their base metal , they are: copper-based alloys (*CuAlNi, CuZnAl, etc*);

nickel-titanium alloys (*NiTiNOL*) and some iron alloys (*FeMnSi, FeNiC,* and *FeNiCoTi*), where the first two groups are best suited for engineering applications. *Nitinol* is well known to be biocompatible, present good operating tension and great deformation recovery. These factors lead these alloys to be considered as the best current options for applications in electromechanical and biomedical systems.

2.2 FUNDAMENTALS OF SHAPE MEMORY ALLOYS

Shape memory alloys are known for having two very specific nonlinear phenomena: the shape memory effect and the superelasticity. Both of these effects arise from a process of martensitic transformation that takes place in the material when a mechanical stress or temperature alteration occurs. In a normal SMA material, three different crystallographic structures may exist. Two of these phases occur at low temperature (twinned martensite and detwinned martensite) and one occurs at high temperature (austenite). This transformation occurs at high speed without atomic diffusion and can be caused both by temperature and mechanical loading applied to the material. The transition between these phases is the source of the effects and behavior presented by SMA materials. Figure 1 shows the common types of crystal structures in an SMA material.

Figure 1 - Austenite and Types of Martensite Present in an SMA Material
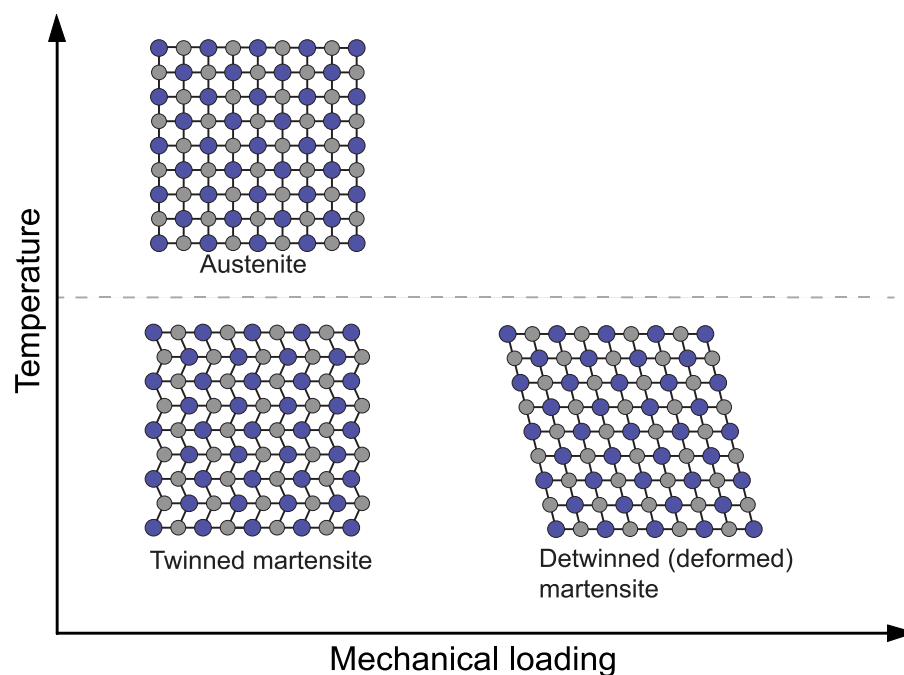
Source: Adapted from Leo (2007)

The SMA material has four well-defined temperatures that control its phase transformation, being: *As* - the start austenitic phase temperature, *Af* - the final austenitic phase temperature, *Ms* - the start martensitic phase temperature and *Mf* - as the final martensitic phase temperature. The exact values of these temperatures depend on the composition of the alloy. Figure 2 shows the hysteresis behavior in the phase transformation of the SMA material, relating the transformation temperatures and the martensitic fraction present in the alloy.

Figure 2 - Martensitic Fraction as a Function of Temperature
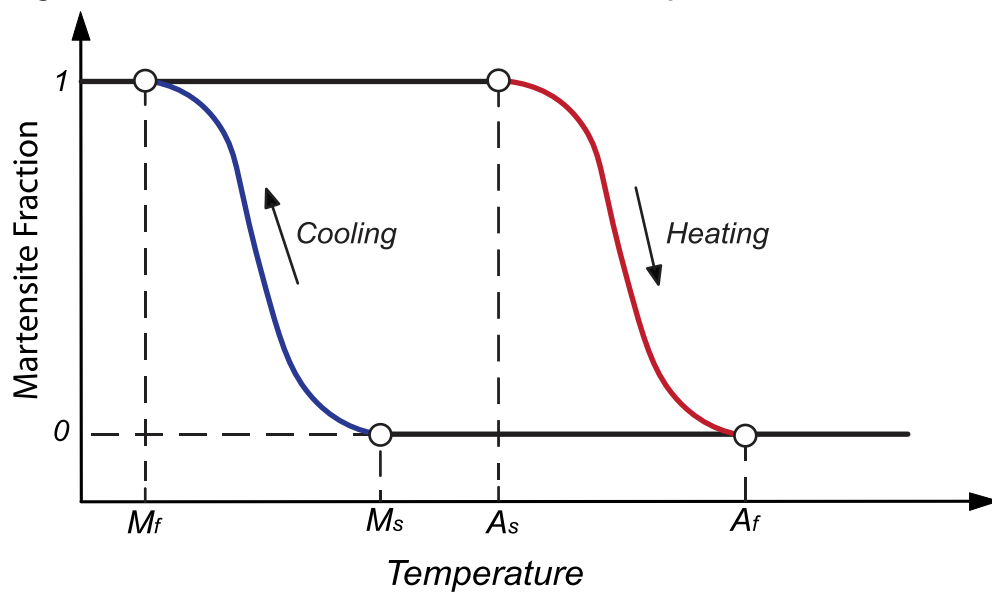
Source: Adapted from Lagoudas (2008)

As shown in Figure 2, when in a completely martensitic phase, the material is considered to have a martensitic fraction with a value equal to 1 (100% martensite and 0% austenite). Increasing the temperature to a value equal to *As*, the material start its phase transformation, where the value of the martensitic fraction will decrease to a final value of 0 (0% martensite and 100% austenite). Thus, in this stage, it is considered that the material has passed completely to the austenitic phase.

In most cases, the temperatures follow the relation presented by Equation (2.1).

$$M_f < M_s < A_s < A_f \tag{2.1}$$

2.2.1 Shape Memory Effect

When the material is deformed plastically in the twinned martensite phase, at a temperature below the austenite phase start temperature (*As*) and is subsequently heated to the final austenite temperature (*Af*), the material will return to its original form that existed previously to the deformation. This is called the Shape Memory Effect (SME). Figure 3 describes this process in a specimen under uniaxial loading in detail using five stages (S1 to S1).

Figure 3 - The Shape Memory Effect in an SMA Material
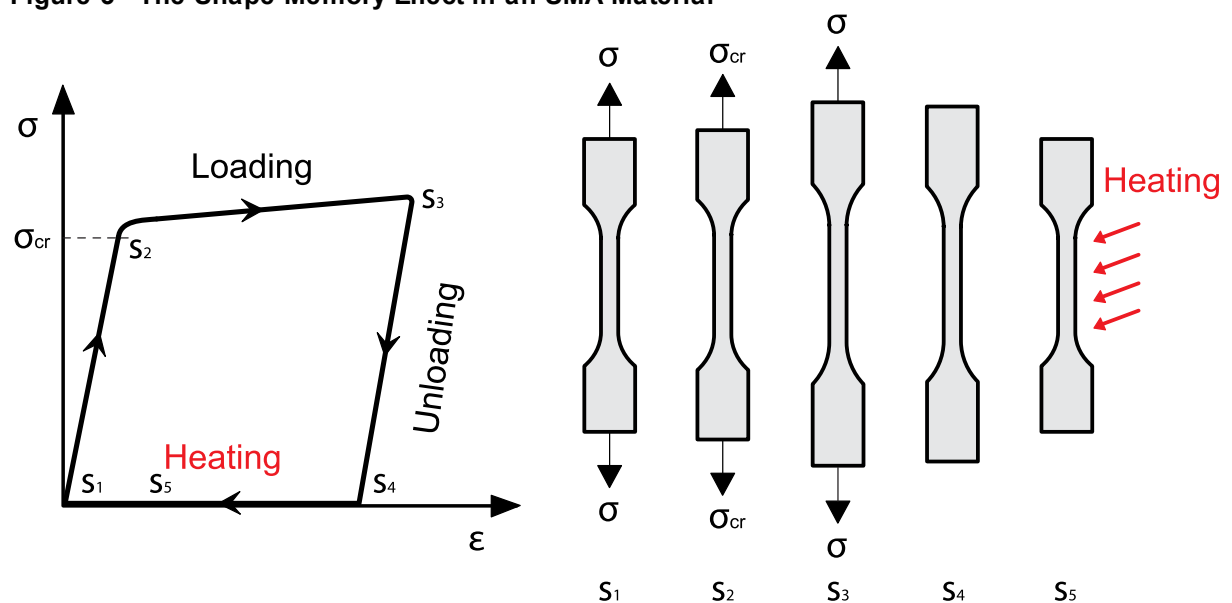
Source: Adapted from Leo (2007)

The process begins in S_1, in this stage, the material is in the temperature where all its structure is in the twinned martensite phase, with no applied mechanical stress. Applying a mechanical load, the material will deform elastically until it reaches a critical stress value (σ_{crit}). After that point (S_2), the material will deform plastically with little variation in the mechanical stress required. Structurally, during this transition, the twinned martensite will become detwinned or deformed martensite (S_3). Now, if all the mechanical stress is removed, the material will retain a great part of this plastic deformation, in other words, the material is deformed (S_4). In this point, if the material is heated to the austenite temperature, a phase transformation will occur, and the detwinned martensite will become austenite, where, in the same process, the material will return to its original form (S_5). If the material is cooled, it will return to a condition identical to that existing in the (S_1), ending the cycle.

As we have this residual strain after unloading the material ($S_3 \rightarrow S_4$), the operation of this effect occurs by a hysteresis graph.

2.2.2 Superelasticity

Superelasticity or pseudoelasticity is the ability of the material to return structurally after undergoing mechanical loading. In SMA materials, this effect occurs due to the martensitic transformation in a specific temperature condition and can recover values greater than 10% of strain. Figure 4 describes this process considering a specimen under uniaxial loading using five stages, a similar process to that presented in the shape memory effect.

Figure 4 - The Superelasticity Effect in an SMA Material
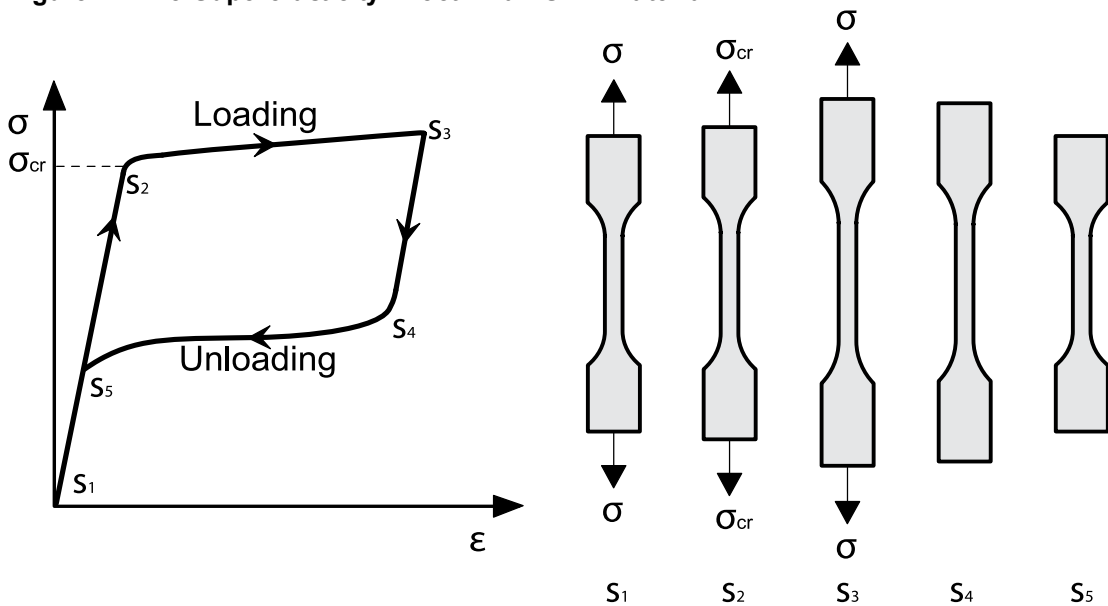
Source: Adapted from Leo (2007)

The process starts at S_1, at this point, the material is at a temperature *Af,* without mechanical loading. The entire structure of the material is considered austenite. Similar to the shape memory effect, after a mechanical load that exceeds a critical value (σ_{crit}), the material will have a high deformation (apparently plastic) without much increase of the applied stress (S_3). In this process, due to the applied stress, the austenite phase becomes detwinned martensite. After that point, if the mechanical stress is removed, the material will return structurally, recovering the strain and becoming austenite again (S_5).

As this effect occurs via a hysteresis diagram, energy dissipation occurs during the process. Therefore, this effect is well considered when it is desired to attenuate or dampen a system (LAGOUDAS, 2008; LEO, 2007).

2.2.3 Characteristics of the Shape Memory Alloy Materials

Shape memory alloy materials demonstrate special characteristics that differentiate them from other smart materials, making them good choices in many types of projects. The most known advantages of the SMA materials are the already mentioned biocompatibility, corrosion resistance, and great strain recovery. Another great advantage is that depending on the alloy, the shape memory effect may occur at different temperatures, where there are alloys operating at low temperatures (below 35ºC) alloys with medium temperatures (75ºC) and alloys for high temperatures (above 100ºC). The ease of merge with other structures can also be considered an advantage, as the material consists only of a metallic alloy, structures of different shapes and sizes can be constructed such as cables, springs or more complex structure.

A major advantage of SMA materials is their power/weight ratio when compared to other types of actuators. Figure 5 shows a comparison of SMA actuators with DC motors, pneumatic actuators, and hydraulic actuators (MAVROIDIS, 2002).

Figure 5 - Comparison between the most Common Actuators
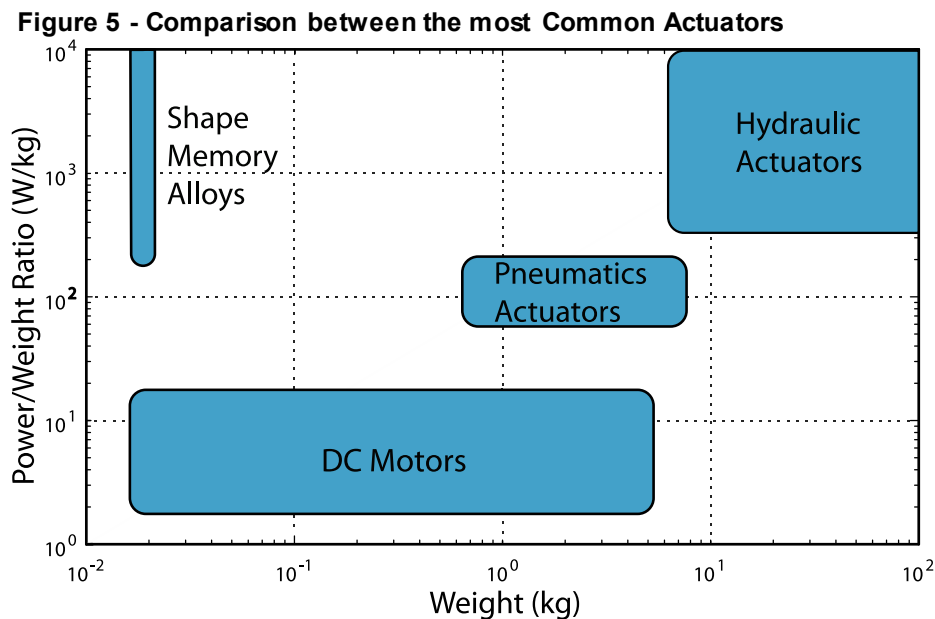
Source: Adapted from Mavroidis (2002)

It can be seen in Figure 5 that the SMA actuators have the best power/weight ratio for low mass actuators. This occurs because of fact that the great majority of the SMA actuators consist only of the shape memory element and some device to make its temperature control. Because of that, this type of actuator presents a low mass/volume when compared to a common actuator (electric, hydraulic or pneumatic) that commonly consists of a more complex system, with more parts and subsystems. This characteristic, allied with a lower energy loss and quiet operation, favors their use in several applications, especially those that require reduced size and weight.

High strain recovery and high-stress capacity is also a positive factor when working with SMA. When compared to other smart materials that can be used as actuators, SMA has one of the highest structural return capacity and actuation stress. This feature favors the use of this type of material in actuators that require high displacements and high forces of actuation. Figure 6 shows a comparison between the SMA materials and other materials classified as smart.

Figure 6 - Intervals for Actuation Stress vs. Strain for Different Materials
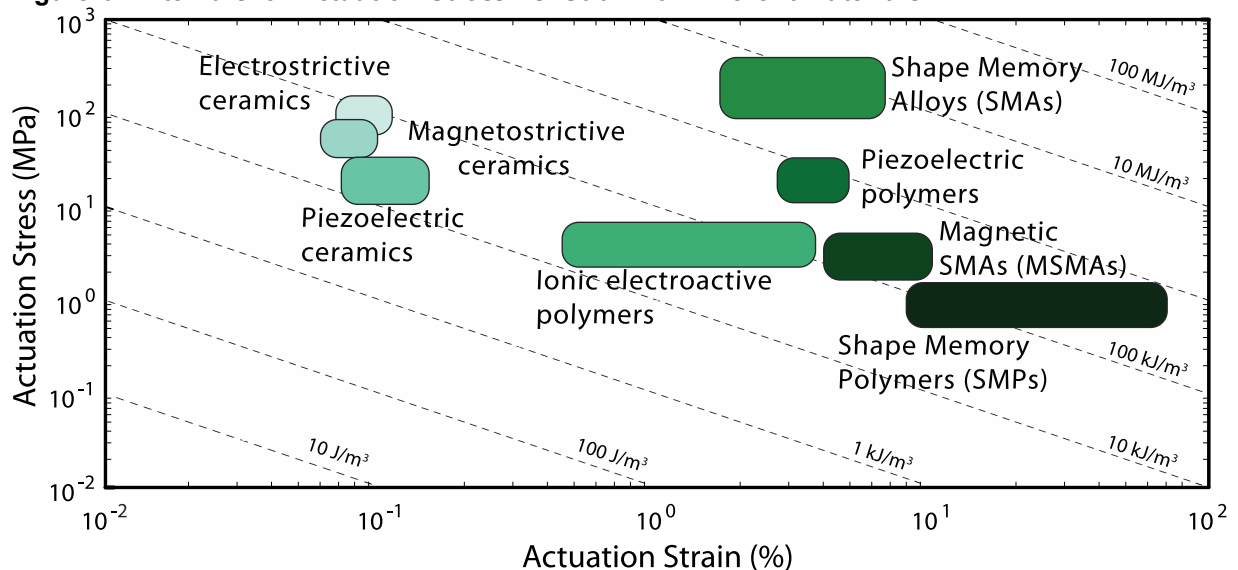
Source: Adapted from Lagoudas (2008)

However, SMA materials have a low actuation frequency when compared to other smart materials. Figure 7 shows a graphical comparison between the frequencies of actuation for each type of material classified as smart. It is clear that the shape memory alloys present one of the smallest values of actuation frequency when in comparison with others materials. This makes this type of material good for applications that require frequencies with values under the 10 *Hz*.

Figure 7 - Specific Actuation Energy Density vs. Actuation Frequency for Different Materials
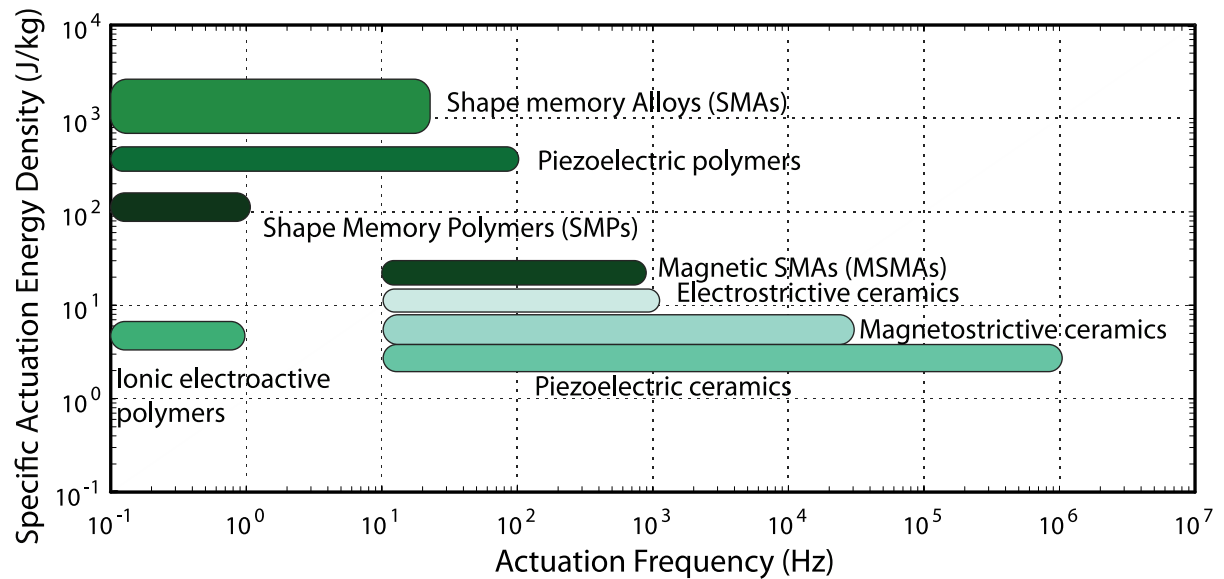
Source: Adapted from Lagoudas (2008)

2.3 PHENOMENOLOGICAL MODELS OF SHAPE MEMORY ALLOYS

Since the beginning of the studies with the SMA materials, several mathematical models tried to represent the effects of SME and/or superelasticity. Due to the very specific and complex characteristics of these materials, such as the occurrence of their effects through a hysteresis graph and the interdependence between stress, strain, and temperature, several mathematical models with very different foundations appeared. According to Paiva and Savi (2006), two types of approaches are used in the great majority of the models: the approach considering the microscopic behavior and the approach considering the macroscopic behavior (phenomenological models).

This work emphasizes the models with assumed phase transformation kinetics, a branch of the phenomenological models since according to some authors (ELAHINIA; ASHRAFIUON, 2002; PAIVA; SAVI, 2006), these models are the most used in experimental studies, presenting great validation or similarity with the real behavior. In this group, the models of Tanaka (1986), Liang and Rogers (1997), Brinson (1993) and Elahinia and Ashrafiuon (2002) stand out. These models use mathematical functions of different types (exponential, cosine, etc.) to describe the phase transformation kinematics of the SMA material. Most of these models are changes in the original model proposed by Tanaka (1986).

To describe the behavior of the SMA material, Tanaka uses four state variables: stress (σ), strain (ε), martensitic fraction (ξ) and temperature (T). These parameters are non-linear and interdependent. The Equation (2.2) shows the relationship between each component.

$$\dot{\sigma} = E\dot{\varepsilon} + \Omega\dot{\xi} + \Theta\dot{T} \tag{2.2}$$

where E is the elastic modulus, Ω is the phase transformation modulus and Θ is the thermoelastic modulus. The great majority of phenomenological models use this equation in this exact form. However, each author proposed a set of equations and conditions for the martensitic transformation curves.

2.3.1 Tanaka's Model

The Exponential Model or Tanaka's Model was proposed by Tanaka and collaborators in 1986. Due to hysteresis present in the SMA material, there are two equations: one for heating and one for cooling. This pattern will also be followed by other researchers.

Two exponential equations are used to obtain the martensitic fraction, one used for the transition from the austenite state to the martensite state (cooling) and another equation for the transition from the martensite state to the austenite (heating) state. Equation (2.3) refers to the cooling effect of the SMA material, also known as direct transformation.

$$\xi_{A \to M} = 1 - \exp\left(-a_{MT}\left(M_s - T\right) - b_{MT}\sigma\right) + \xi_0 \tag{2.3}$$

The Equation (2.3) is valid only for mechanical stress values (σ) given by Equation (2.4).

$$\sigma \geq \left(\frac{a_{MT}}{b_{MT}}\right)(T - M_s) \tag{2.4}$$

The constants present in Equations (2.3) and (2.4) can be obtained from Equation (2.5).

$$a_{MT} = -\frac{2\ln(10)}{M_s - M_f}, \quad b_{MT} = -\frac{2\ln(10)}{C_M} \tag{2.5}$$

The Equation (2.6) shows the behavior during the heating of an SMA alloy, also known as the reverse effect.

$$\xi_{M \to A} = \xi_0 \exp\left(-a_{AT}\left(T - A_s\right) - b_{AT}\sigma\right) \tag{2.6}$$

The Equation (2.6) is only valid for stress values given by Equation (2.7).

$$\sigma \le \left(\frac{a_{AT}}{b_{AT}}\right)(T - A_s) \tag{2.7}$$

where the constants of Equations (2.6) and (2.7) are given by Equation (2.8).

$$a_{AT} = \frac{2\ln(10)}{A_f - A_s}, \qquad b_{AT} = \frac{2\ln(10)}{C_A} \tag{2.8}$$

The Tanaka model does not mention a specific equation for the strain tensor, what is generally considered in the literature is to isolate the deformation term from Equation (2.2), as shown in Equation (2.9).

$$\dot{\varepsilon} = \frac{\dot{\sigma}}{E} - \frac{\Omega}{E}\dot{\xi} - \frac{\Theta}{E}\dot{T} \tag{2.9}$$

Thus, the deformation of the SMA material is dependent to a portion related to the stress, a portion related to the martensite fraction and the last portion related to the temperature of the material.

The Tanaka model does not consider a distinction between twinned martensite and detwinned martensite, this leads to an uncertain behavior when considering low temperatures.

2.3.2 Model of Liang & Rogers

The Liang and Rogers model (1990) consists of an evolution of the model proposed by Tanaka. In this new model, the exponential equations proposed by Tanaka for the cooling and heating of the SMA material are replaced by equations with cosine functions. This new proposal presents a more similar behavior with the actual hysteresis curve presented by the SMA material. The equation that relates the stress, deformation, martensitic fraction and temperature remains the same to that presented by Equation (2.2).

The Equation (2.10), for the one-dimensional model of Liang and Rogers, describes the evolution of the material from the austenite phase to the martensite phase, ie, the equation for cooling.

$$\xi_{A \to M} = \frac{1 - \xi_0}{2} \cos\left(a_{ML}\left(T - A_f - \frac{\sigma}{C_M} \right) \right) + \frac{1 + \xi_0}{2} \qquad (2.10)$$

New equations were stipulated for the stress limit of the transformation. The Equation (2.11) defines the stress values for which Equation (2.10) is valid.

$$C_M(T - M_s) < \sigma < C_M(T - M_f) \qquad (2.11)$$

Equation (2.12) describes the evolution of the martensitic transformation in the process of heating.

$$\xi_{M \to A} = \frac{\xi_0}{2}\left(\cos\left(a_{AL}\left(T - A_s - \frac{\sigma}{C_A} \right) \right) + 1 \right) \qquad (2.12)$$

where the limit for the process to occur is given by the Equation (2.13).

$$C_A(T - A_f) < \sigma < C_A(T - A_s) \qquad (2.13)$$

Two new constants appear, a_{AL} and a_{ML}, being given by the Equation (2.14).

$$a_{AL} = \frac{\pi}{A_f - A_s}, \quad a_{ML} = \frac{\pi}{M_s - M_s} \qquad (2.14)$$

2.3.3 Brinson's Model

Brinson (1993) proposed a division between the functions that provide the martensitic fraction into two parts: one part that comes from the stress, and another part that comes from the temperature. Equation (2.15) shows this new approach.

$$\xi = \xi_S + \xi_T \qquad (2.15)$$

where the subscript S is for stress and T is for temperature.

This addition allows the model to cover a higher range of operating temperatures. Three new conditions for martensitic transformation were proposed, where two are for the transformation of austenite to martensite and one for the transformation of the martensite to austenite.

Considering the transformation process of austenite to martensite, when $T < M_s$ and $\sigma_s^{cr} < \sigma < \sigma_f^{cr}$ we have the first condition, where the Equation of transformation is given by Equation (2.16).

$$\xi_S = \frac{1-\xi_{S0}}{2}\cos\left\{\frac{\pi}{\sigma_s^{cr}-\sigma_f^{cr}}\left[\sigma-\sigma_f^{cr}-C_M(T-M_s)\right]\right\}+\frac{1+\xi_{S0}}{2}$$

and
(2.16)

$$\xi_T = \xi_{T0} - \frac{\xi_{T0}}{1-\xi_{S0}}(\xi_S - \xi_{S0})$$

The second set of Equations (2.17), are used when $M_f < T < M_s$ and $\sigma_s^{cr} < \sigma < \sigma_f^{cr}$.

$$\xi_S = \frac{1-\xi_{S0}}{2}\cos\left[\frac{\pi}{\sigma_s^{cr}-\sigma_f^{cr}}(\sigma-\sigma_f^{cr})\right]+\frac{1+\xi_{S0}}{2}$$

and
(2.17)

$$\xi_T = \xi_{T0} - \frac{\xi_{T0}}{1-\xi_{S0}}(\xi_S - \xi_{S0})+\Delta_{T\xi}$$

If $M_f < T < M_s$ and $T < T_0$,

$$\Delta_{T\xi} = \frac{1-\xi_{T0}}{2}\left\{\cos\left[a_M(T-M_f)\right]+1\right\} \text{ else } \Delta_{T\xi} = 0$$

(2.18)

Considering the process that occurs from martensite to austenite, the condition for this happening is $T > A_s$ and $C_A(T-A_f) < \sigma < C_A(T-A_s)$. The Equation (2.19) provides the martensitic fractions for this condition.

$$\xi_S = \frac{\xi_0}{2}\left\{\cos\left[a_A(T-A_s-\frac{\sigma}{C_A})\right]+1\right\}$$

and
(2.19)

$$\xi_T = \xi_{S0} - \frac{\xi_{S0}}{\xi_0}(\xi_0 - \xi)$$

2.3.4 Elahinia's Enhanced Phenomenological Model

The Elahinia's model or enhanced model was developed by Elahinia and Ashrafiuon (2002). This model is an adaptation of the model created by Tanaka and improved by Liang and Brinson. Elahinia questioned the behavior of phenomenological models when it was considered a real dynamical system.

The same constitutive equation of Tanaka (1985) was used by Elahinia, where the Young's modulus was considered to be dependent on the martensitic fraction of the material.

$$\dot{\sigma} = E(\xi)\dot{\varepsilon} + \Omega\dot{\xi} + \Theta\dot{T} \tag{2.20}$$

The equation (2.21) shows the relation of Young's modulus with the martensitic fraction of the material.

$$E(\xi) = E_A + \xi(E_M - E_A) \tag{2.21}$$

where A and M are the subscripts for the crystallographic phase of austenite and martensite, respectively.

The phase transformation model adopted by Elahinia was the same proposed by Liang and Rogers and previously shown in Equations (2.10) and (2.12); however, new conditions for the heating and cooling process were adopted. These new conditions include the effect of complex thermomechanical loadings on the material during the heating and cooling processes.

The new condition for the reverse transformation (heating process) is given by Equation (2.22).

$$\begin{cases} \dot{T} - \dfrac{\dot{\sigma}}{C_A} > 0 \\ \text{and} \\ A_s + \dfrac{\sigma}{C_A} < T < A_f + \dfrac{\sigma}{C_A} \end{cases} \tag{2.22}$$

In a similar way, the new conditions for the occurrence of the forward transformation (cooling process) are given by Equation (2.23).

$$\begin{cases} \dot{T} - \dfrac{\dot{\sigma}}{C_M} < 0 \\ \text{and} \\ M_f + \dfrac{\sigma}{C_M} < T < M_s + \dfrac{\sigma}{C_M} \end{cases} \tag{2.23}$$

As stated by Elahinia, this adapted model is reduced to the model of Liang and Rogers in case the system is isostress or reduced to the Brinson model in case the system is isothermal, that being so, these new conditions proposed by Elahinia unite the Liang & Rogers and Brinson models into a single one.

2.4 SUMMARY

Smart materials are a great alternative in the design of new systems as well as in the optimization of the existing ones. This is possible because these materials have additional characteristics to the common materials and thus, can be used as sensors and/or actuators causing little change in the system.

Among these materials, are the shape memory alloys (SMA). Metal alloys that have two distinct effects that arise when the material undergoes a temperature and/or a mechanical force change, these effects are the shape memory effect and superelasticity effect. Due to the high capacity of work and its simplicity, this type of actuator has been widely studied and implemented in several types of devices and systems. These two effects occur through a process called martensitic transformation, with the material alternating between crystallographic structures as it undergoes mechanical or thermal loading.

Over time, equations that represent the effect of shape memory and/or superelasticity have emerged. We highlight the phenomenological models, having its first model proposed by Tanaka in 1985. With time, other researchers proposed improvements in the Tanaka's model, highlighting the models of Liang and Rogers, Brinson and Elahinia.

3 CHARACTERIZATION OF THE SMA ACTUATOR

The main purpose of this chapter is to acquire the constitutive parameters and to observe experimentally the specific behavior of a shape memory alloy actuator. An acquisition system with a specimen was described and built. Fiber optic sensors were used to obtain the temperature of the specimen, this being one of the most important physical parameters in the study of shape memory alloys. Tests were performed considering a standard pre-loading in the material, where the material was heated through the passage of an electric current. As results, characteristic curves of the material are made and analyzed focusing on the temperature and displacement graphs.

3.1 MOTIVATIONS

The characterization of the system that will be implemented is an important design step in an engineering project. As the SMA material has properties that vary according to its composition, heat treatment, and training, some properties such as transition temperature and necessary factors for the constitutive equations must be obtained experimentally. In addition to providing results that are closer to the real one, numerical simulations with a more refined mathematical model can be used to extend the applications in which these materials can be used. Thus, allowing to quickly investigate a large number of system configurations, predicting behaviors and situations of real systems.

3.2 EXPERIMENTAL PROCEDURE OF THE CHARACTERIZATION

3.2.1 Experimental Setup

A specific system was built for the characterization of the SMA actuator used in this thesis. The system consists of an aluminum frame, where an SMA specimen is fixed vertically. The SMA specimen from Dynalloy ® has 375 *µm* of diameter and 100 *mm* in length. On its lower end, a standard weight of 500 *g* is attached; the weight is responsible for the pre-load needed for the actuator. A capacitive non-contact sensor

is used to measure the displacement of the weight and consequently the strain of the actuator. A power source is used to control the temperature of the SMA material through the passage of an electric current. All the data were obtained through the use of an *NI Daq* model 6212, where the data was processed in a program made on the Labview® software. Figure 8 shows the described apparatus.

Figure 8 - Experimental System Used for the Tests
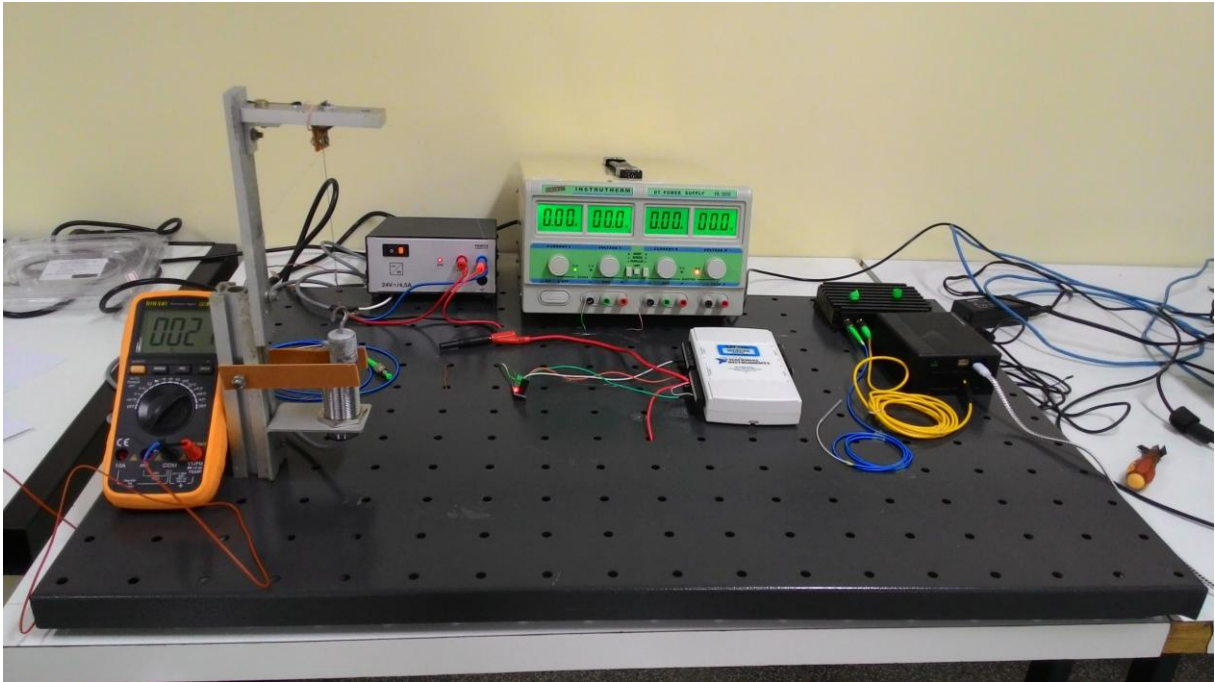
Source: Self-Authorship

Obtaining the exact temperature values of a wire type SMA actuator is a major challenge because of its small diameter. This physical characteristic results in a low thermal mass and little contact area necessary for the more common sensors. To solve this problem, in this thesis, a Fiber Bragg Grating (FBG) was used to obtain the temperature values in a real time of the SMA material. This fiber optic sensor used has a diameter of 400 *μm*, thus exerting little influence on the SMA material.

For the treatment of the experimental data, a Moving Average (MA) filter was projected and used on all the results of the displacement and electrical current. This Low Pass Filter (LPF) was used to remove the unwanted noise coming from the power grid, turning the signal smoother. The filter was designed taking into consideration the 60 *Hz* power grid and the 1 *kHz* acquisition rate of the data acquisition system.

3.2.2 Experimental Results

For the tests, initially, a pre-loading was applied to the material for the complete transformation of the crystallographic structure into detwinned martensite. In the sequence, cycles of different electrical voltages were applied to the actuator. Each test consisted of turning on the power source with a certain pre-set voltage. The material was then heated for a determined time and then, the power source was turned off, allowing the SMA material to cool by natural convection.

The electrical voltage applied to the actuator causes the material to heat up due to the passage of an electric current (Joule Effect) and this causes a change in the martensite fraction of the material. As the temperature increases, it is noticed that the material begins its recovery from the deformation undergone by the preload. The recovery becomes apparent when the temperature of the material reaches the final temperature of the austenite phase A_f.

For the acquisition of the results, were tested voltage values between 0.5 and 1.3 *volts*, considering increments of 0.1 *volts*. These values were chosen based on experimental tests and recommendations of the SMA manufacturer. Table 1 shows the parameters of the actuator.

Table 1 - Properties of the SMA Actuator

Parameter	Value	Unit
R_A	13	Ω
R_M	15	Ω
Diameter	375	μm
Length	0.1	m

Source: Self-Authorship

As the value of the electrical voltage is fixed, it is possible to see a little alteration in the electric current consumption during the heating process. In order to observe this variation, graphs of the electric current consumption were obtained for each electric voltage value applied to the specimen.

Figure 9 shows the behavior of the system with the applied voltages, and Figure 10 shows the electric current consumed by the actuator in every test.

Figure 9 - Deformation Recovery of the Actuator for Every Voltage Applied

(a) 0.8 V

(b) 0.9 V

(c) 1.0 V

(d) 1.1 V

(e) 1.2 V

(f) 1.3 V
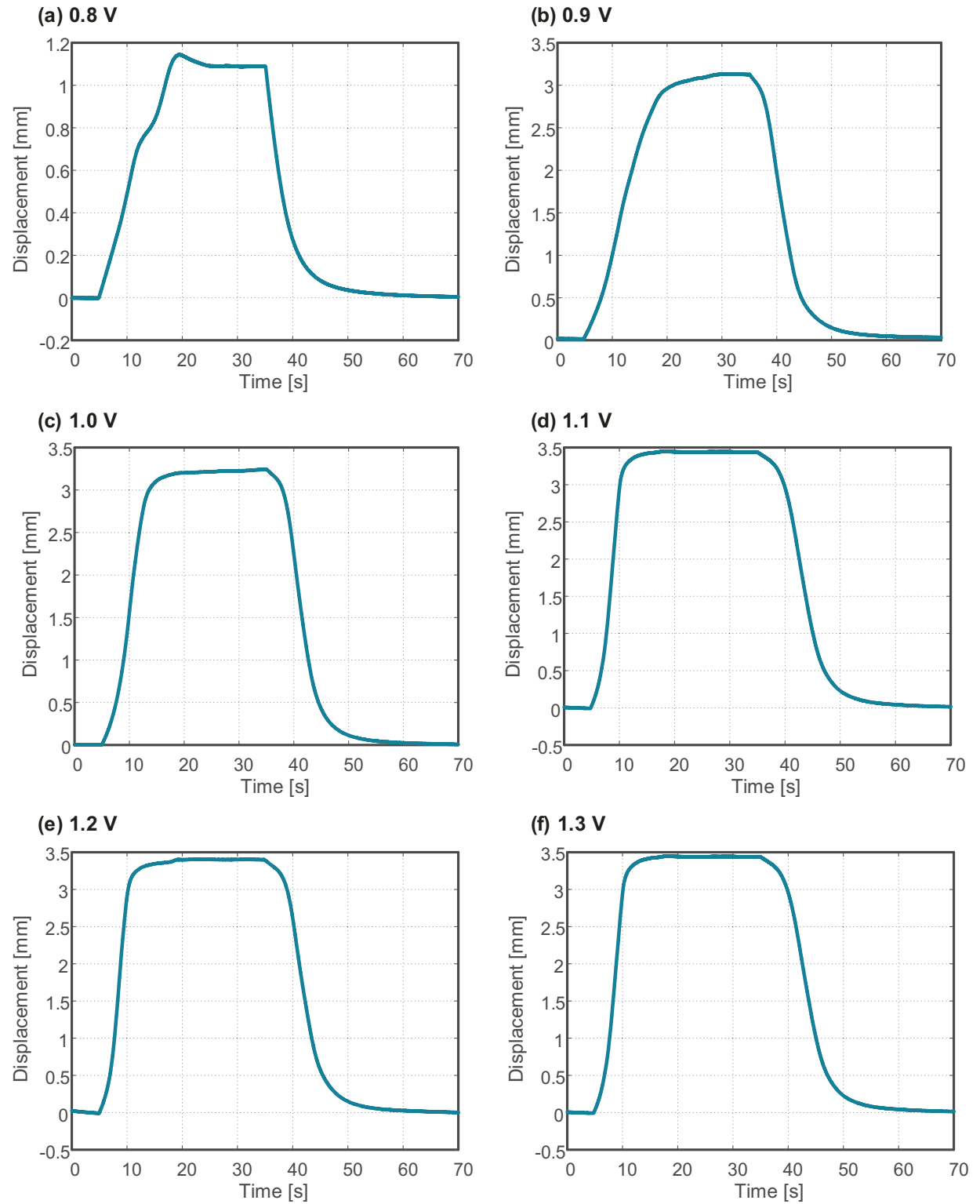
Source: Self-Authorship

Figure 10 - Electric Current in the Actuator Based in the Electric Voltage Applied

(a) 0.8 V

(b) 0.9 V

(c) 1 V

(d) 1.1 V

(e) 1.2 V

(f) 1.3 V
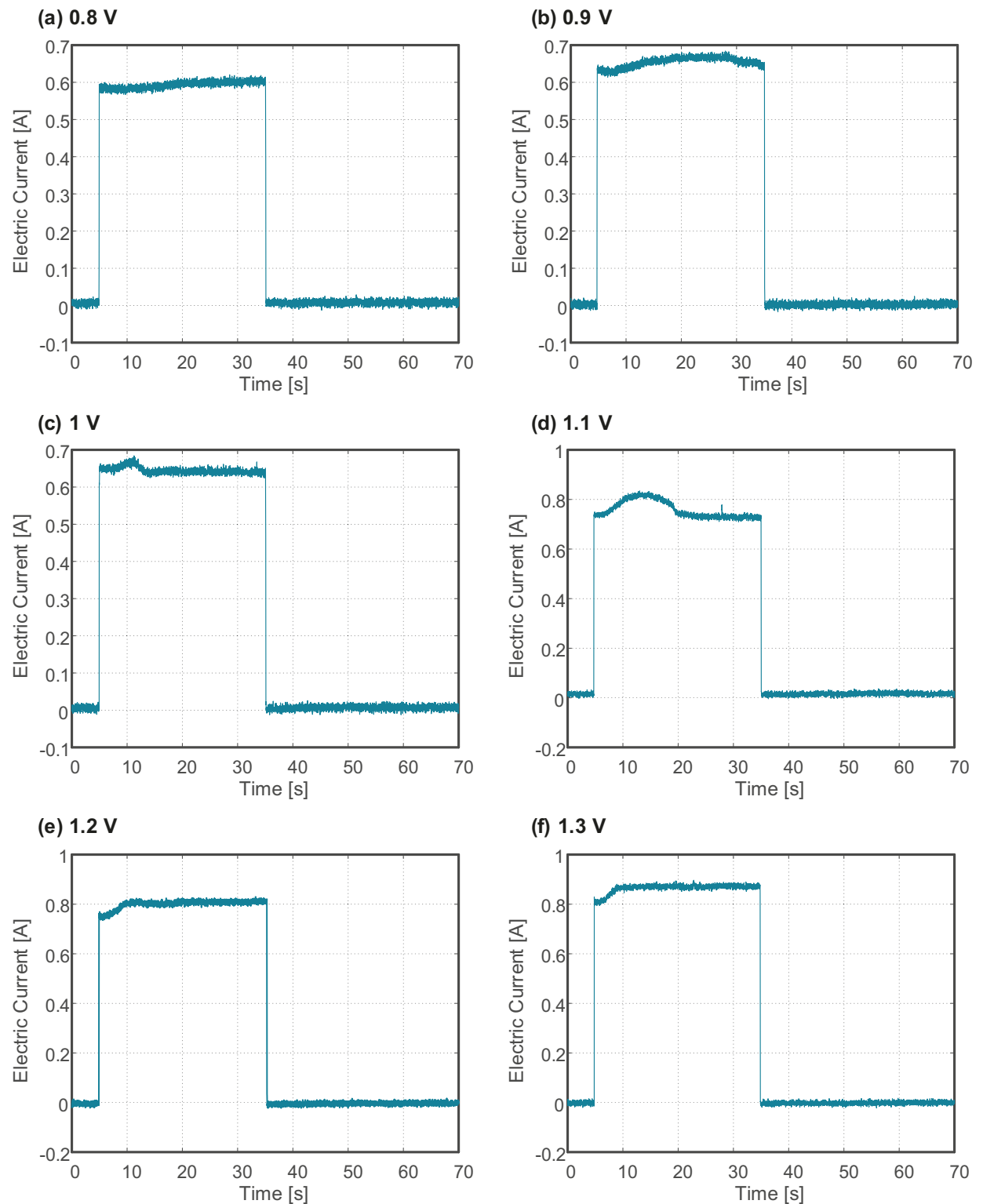
Source: Self-Authorship

As can be seen in Figure 9, for values of electric voltage below 1.1 V it is not possible to assert the level of transformation undergone by the material. At these voltage values, the temperature of the material is not enough to fully transform the crystallographic structure of the actuator, where it is possible to observe the variation

of the deformation recovery. From the values above 1 V, all the higher electrical voltage values give very similar results, showing that all the structure of the material has reached the A_f temperature. Analyzing the results of the electric currents, it is noticed that the values of the currents do not remain constant during the process of heating. This occurs due to changes in the electrical resistance of the SMA material during the heating and cooling process.

Figure 11 shows a comparison with all the tests made for the displacement of the actuator. Also, are shown results for electrical voltages below 0.8 *V*.

Figure 11 - Behavior of the Actuator for the Heating and Cooling Processes
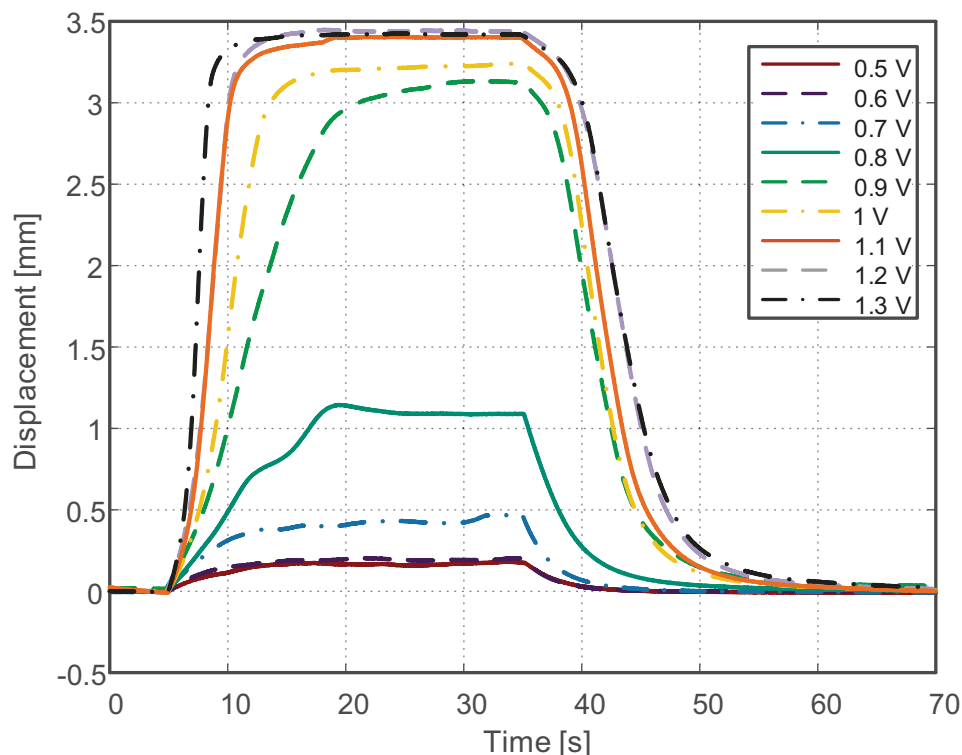
Source: Self-Authorship

Figure 12 presents the points of maximum displacement for each value of applied electric voltage. Together with the results presented by Figure 11, it is possible to notice that the SMA material used passes completely from the phase of detwinned martensite to austenite at the voltage value of 0.9 *V* and that the values above only accelerate the transformation. This value of electric voltage corresponds almost to a value of 690 *mA* of electric current, being a relatively high value. However, as the voltage is low, the total power consumption of the circuit could be considered also a low value.

Figure 12 - Displacement of the Actuator for Each Electric Voltage Value
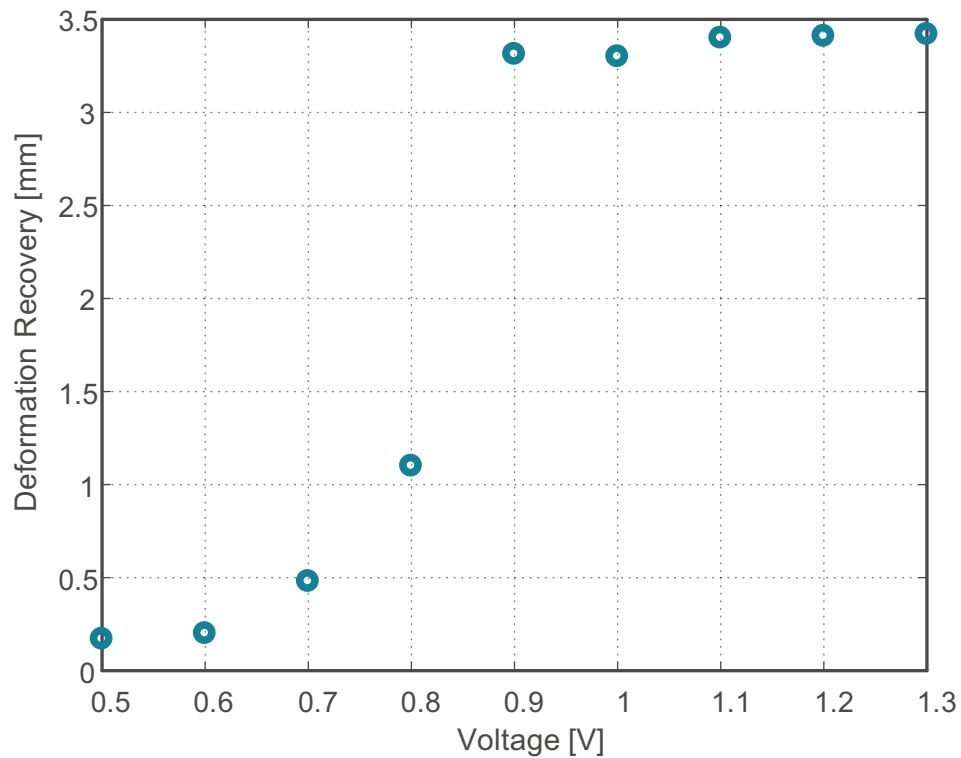
Source: Self-Authorship

Figure 13 presents repetitions of the same tests for voltage values of (a) 1.2 *V* and (b) 1.3 *V*. This type of result shows how the SMA material presents differences during its operation when tests are repeated, where with the same voltage applied, its possible to see differences in the displacement of the material.

Figure 13 - Displacement of the Actuator for Each Electric Voltage Value

(a) 1.2V   **(b) 1.3 V**
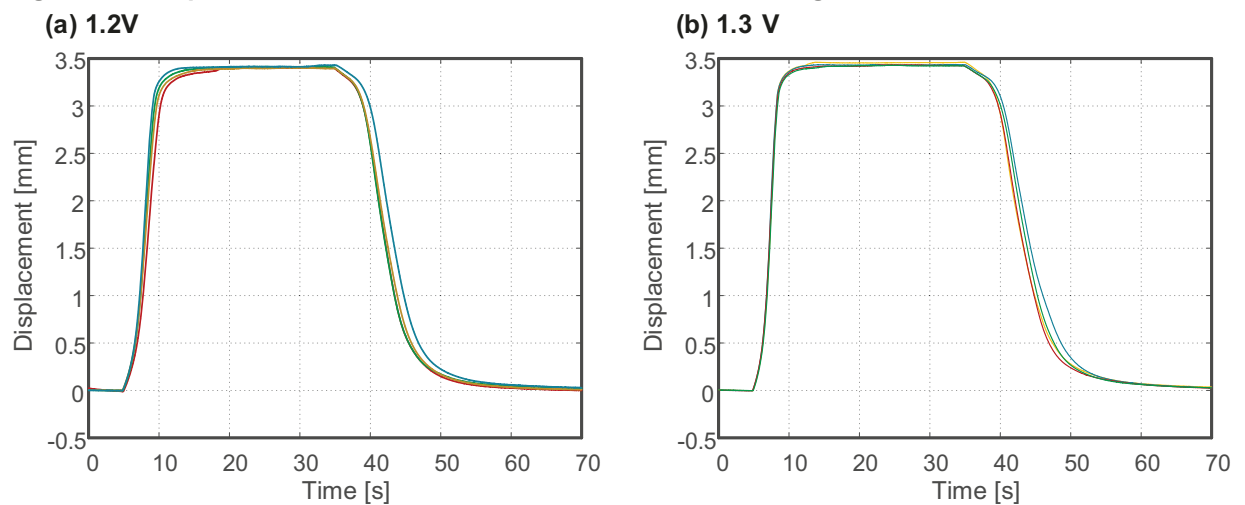
Source: Self-Authorship

This same result was shown by Elahinia (2004), and according to the author, is caused by non-uniform heating of the actuator.

3.2.3 Heat Transfer Model

An existing problem when working with SMA actuators is the temperature control. Typically, the heating process of the SMA actuator is made by passing an electric current (Joule effect or Ohmic heating) in the actuator. However, as the actuator often consists of a wire, its reduced dimension makes it difficult to obtain its experimental temperature.

In the characterization part of the actuator was used an ultra-sensitive fiber optic sensor to obtain the temperatures, but this possibility does not always exist, especially when the physical quantity must be quickly obtained. For these situations, an equation that gives the temperature of the actuator wire becomes useful.

Figure 14 shows a wire with diameter d_w and length l_w. Joule heating is the process of heating a material by passing an electric current i_{act}, where this current is generated by the electric voltage drop V_{act}.

Figure 14 - SMA Actuator Heated by the Passage of an Electric Current
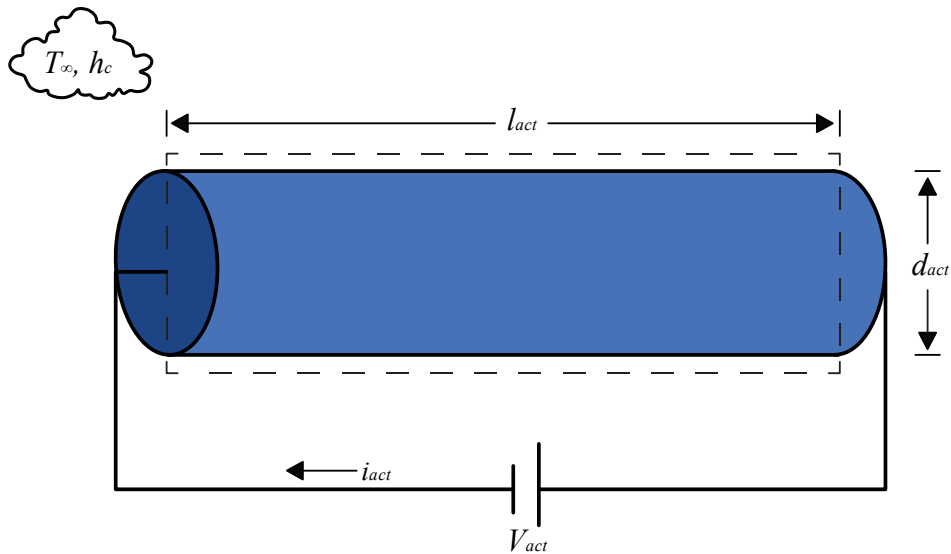
Source: Self-Authorship

Considering uniform temperature throughout the actuator, the constant ambient temperature during the process and only the effects of convection and conduction, it is possible to obtain the heat transfer equation for the actuator material.

$$mc_p \frac{dT}{dt} = \underbrace{I_{act}^2 R_{act}}_{geration} - \underbrace{h_c A_c (T_{sf} - T_\infty)}_{convection} \qquad (3.1)$$

where T_{sf} is the surface temperature of the material, T_∞ is the ambient temperature, m is the specific mass and c_p is the specific heat of the material, the convection heat transfer is given by h_c and A_c is the circumference area of the wire.

To obtain the value of the convection coefficient, the proposal presented by Gori, Serrano, and Wang (2006) was used. In this approach, the SMA wire is considered as a heated thin cylinder. Making this consideration, the number of Nusselt is given by Equation (3.2).

$$Nu = \frac{4}{3}\left[\frac{7Ra\,\mathrm{Pr}}{5(20+21\mathrm{Pr})}\right]^{1/4} + \left[\frac{4(272+315\mathrm{Pr})}{35(64+63\mathrm{Pr})}\right]\frac{l_{act}}{D_{act}} \tag{3.2}$$

where Ra is the Rayleigh number and can be obtained by using the Equation (3.3).

$$Ra = \frac{g\beta\Delta T l_{act}^{\,3}}{\alpha\upsilon} \tag{3.3}$$

where g is the gravitation acceleration, α is the thermal diffusivity, υ is the kinematic viscosity and $\beta = 1/T$.

The number of Nusselt can be related to the coefficient of heat transfer by using the following Equation.

$$h_c = \frac{kNu}{l_{act}} \tag{3.4}$$

All the parameters for the calculations are shown in Table 2, with all air properties at the film temperature (CENGEL; GHAJAR; KANOGLU, 2011).

Table 2 - Properties of the Air

Temperature of the Surface (°C)	Thermal Conductivity (W/m.K)	Thermal Diffusivity (m^2/s)	Kinematic Viscosity (m^2/s)	Prandtl Number
33	0.02551	2.14e-05	1.56e-05	0.7296
39	0.02588	2.21e-05	1.61e-05	0.7282
46	0.02625	2.28e-05	1.66e-05	0.7268
58	0.02662	2.35e-05	1.70e-05	0.7255
73	0.02730	2.48e-05	1.78e-05	0.7230
75	0.02734	2.487e-05	1.79e-05	0.7229
80	0.02738	2.49e-05	1.81e-05	0.7220
93	0.02800	2.63e-05	1.89e-05	0.7210
101	0.02820	2.69e-05	1,92e-05	0.7100

Source: Values interpolated from Cengel, Ghajar and Kanoglu (2011)

Using the parameters from the Table 2 and the Equations (3.2), (3.3) and (3.4), it is possible to obtain the values for the heat transfer coefficient considering every surface temperature. For the value of the electric resistance R_{act}, was used the R_M value for every electric voltage below 1V, a value which is considered that most of the material changed phase to austenite. The value of the R_{act} was changed to R_A for the values of voltage equals to 1.0V, 1.1 V, 1.2 V and 1.3 V. Figure 15 shows the values of h_c for each voltage applied to the actuator.

Figure 15 - Heat Transfer Coefficient for Every Voltage Applied
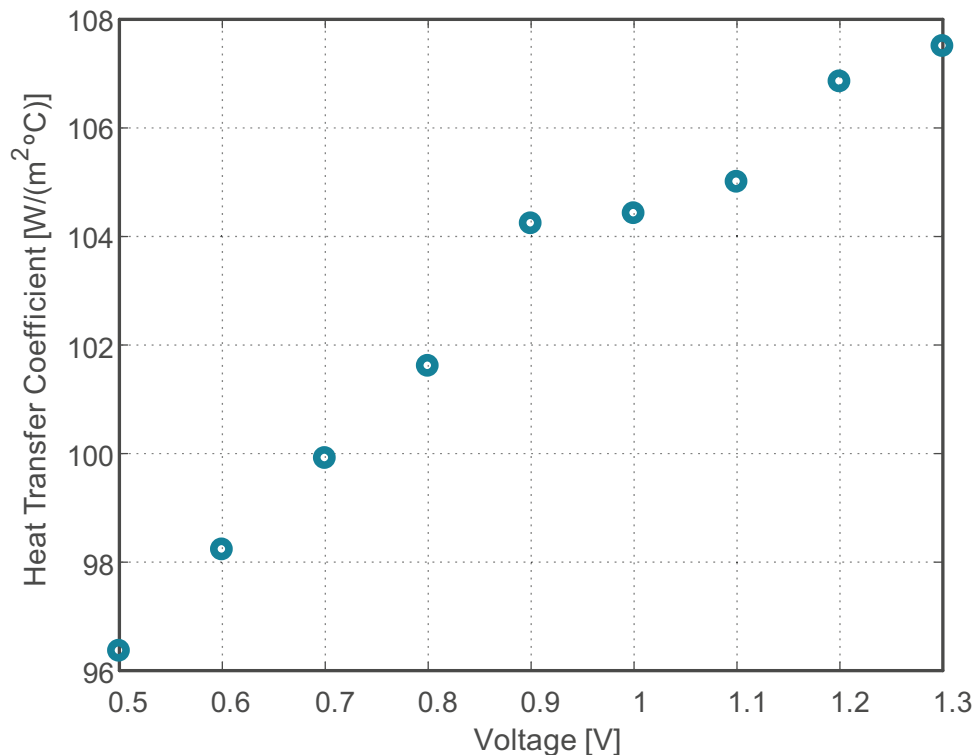
Source: Self-Authorship

The heat transfer coefficient presents a completely linear profile. Where, with the increase of the temperature, the coefficient also increases in a similar way. It is also noticed that the coefficient does not have a very vertiginous increase with the complete transition of the material to the austenite crystallographic phase.

Figure 16 presents a comparison of all the temperatures experimentally obtained with the model of the Equation (3.1). The results of Figure 16 show that the values obtained for the parameters of the SMA material provide simulations results very close to the actual behavior of the actuator. But it must be remembered that

calculations involving natural convection tend to present great uncertainties, especially in the case of Equation (3.2), that is derived from experimental systems.

Figure 16 - Comparisons between the Experimental and Calculated Temperatures
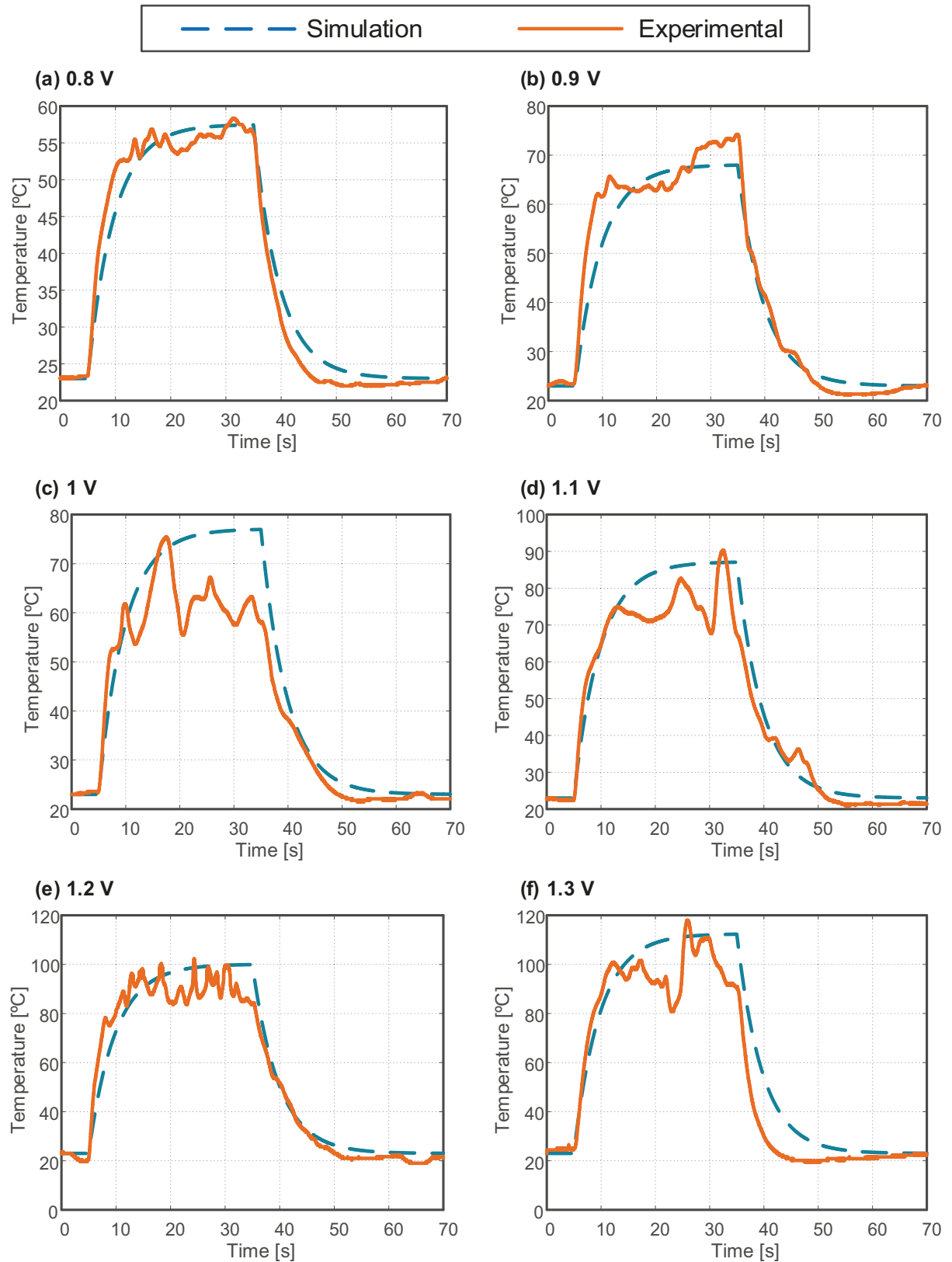
Source: Self-Authorship

3.3 SUMMARY

An important step in implementing an actuator is the complete understanding of its behavior in a real system. In this chapter, a system was built in order to observe the behavior of an SMA material. This experimental system consisted of an SMA actuator fixed at one of its ends. Electrical voltages with pre-defined values were applied in the material. Through the Joule effect, the voltage drop generates an electric current that flows through the material and, because of the internal electrical resistance, generates heat. The behavior of the actuator was analyzed through displacement graphs generated by the recovery of his deformation and temperature graphs. The temperature results were obtained through the implementation of an optical fiber sensor.

The results show the material recovery over time in comparison to the applied electric voltage, where it is clearly perceived that the material requires considerable time to act. With the results of the temperatures, the coefficient of heat transfer was obtained through a proper equation and later was used to simulate the temperatures and the thermal behavior of the material during the heating and cooling processes.

4 NON-IDEAL SYSTEM

This chapter presents the basic concepts of the non-ideal systems and the process to obtain the mathematical model for the system under study. The non-ideal system chose consists of a cantilever beam and an unbalanced DC motor that is responsible for the excitation of the dynamical system. The equation of the non-ideal system was obtained using the Lagrange's formalism, where it was considered the coupling of the dynamical system with the complete equation of the electric motor. Numerical simulations with parameters from the experimental system are performed in order to obtain the Sommerfeld effect in the system.

4.1 THE NON-IDEAL SYSTEMS

When the energy source acts in a mechanical structure but is not considered the performance of the structure in the energy source, the system receives the classification of ideal. Conversely, when is considered the dynamics of the structure in the energy source, the system receives the classification of non-ideal. In this type of system, the equations related to the energy source are derived together with the equations related to the movement of the structure, turning the analysis more complete and also more complex (BALTHAZAR et al., 2003).

The first non-ideal type system was studied by Arnold Sommerfeld in 1902. When studying a structure composed of a cantilever beam and an unbalanced electric motor at its free end, Sommerfeld realized that the system underwent certain dynamic instability when the system approached the resonance region, returning to a normal behavior after the passage of this region. What happened was an exchange of energy between the electric motor and the mechanical structure. The motor at the same time that excited the structure, suffered influence of itself, losing energy that was only converted into mechanical vibration. This causes a discontinuity of the linear curve of rotation of the motor as a function of the applied energy. After the passage of the resonance region, the system returns to works normally and the vibration amplitudes fall abruptly. This effect was later known as Sommerfeld effect, jump effect or jump phenomenon, being studied as one of the first effects that arise in systems classified as non-ideal (BALTHAZAR et al., 2003).

After the discovery, some authors wrote about the specific effects of this dynamic system type. Kononeko (1969) wrote a complete book on the subject. Balthazar et al. (2003) made a review of the main types of non-ideal systems as well as their basic characteristics and mathematical considerations. Some works have also focused on dealing with the control of this type of phenomena (PICCIRILLO; TUSSET; BALTHAZAR, 2014) because, in addition to causing the loss of energy used in the system, the effects of mechanical vibration can be quite severe.

According to Fenili (2000), when considering a non-ideal system, some important characteristics and effects that arise are: presence of abrupt changes in the displacement amplitudes of the structure, where this variation is very sensitive to changes in the voltage of the motor, this effect being the Sommerfeld effect or jump phenomenon; discontinuity of the amplitude versus frequency curve and dependence of these effects with the electromechanical characteristics of the motor.

The non-ideal behavior can appear in a great plethora of systems. However, in the sequence of this master's thesis, the classic problem consisting of a cantilever beam and an electric motor is mathematically modeled and numerically simulated.

4.2 MATHEMATICAL MODELING

The chosen system is composed of a cantilever beam and an unbalanced DC (Direct Current) motor fixed at its free end. This is a classic non-ideal system. Figure 17a shows a schematic of the real system and Figure 17b shows the equivalent lumped-parameter system considered for the mathematical model, where it should also be noted that the coordinate system has been changed.

In Figure 17, k and c are the stiffness and the viscous damping of the mechanical structure, respectively. M is the total mass of the system, being the sum of the beam mass and motor mass. J is the moment of inertia from the mechanical parts of the electric motor, r is an eccentricity of the shaft and m is the unbalanced mass.

In this thesis, the system model is obtained using the Lagrange formalism. In this method, instead of forces (Newton's Laws of Motion), the energies present in the system are used. The kinetic energy (E_k) and the potential energy (E_p) of the system are related by the Equation (3.5).

Figure 17 - Non-Ideal System. (a) Real System. (b) Lumped-Parameter System

a)   b)
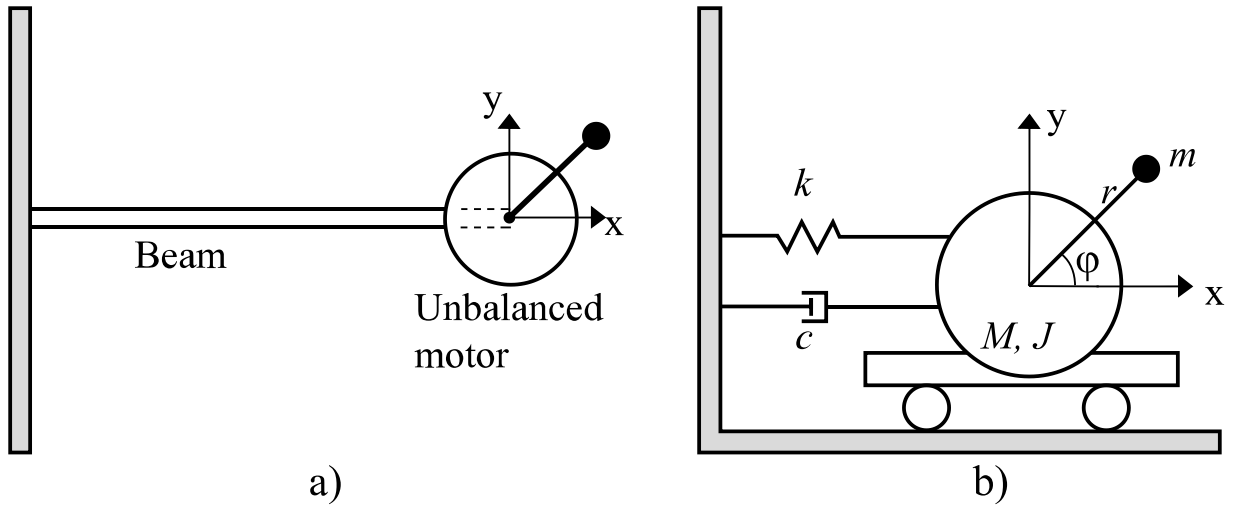
Source: Adapted from Balthazar et al. (2003)

$$L_g = E_k - E_p \tag{3.5}$$

where L_g is the Lagrange function. The dynamical system's equations could be obtained using the relation presented in Equation (3.6).

$$\frac{d}{dt}\left(\frac{\partial L_g}{\partial \dot{q}_i}\right) - \left(\frac{\partial L_g}{\partial q_i}\right) + \left(\frac{\partial D}{\partial \dot{q}_i}\right) = Fe \quad \text{for } i = 1, 2, 3 \dots N \tag{3.6}$$

where q_i is a set of generalized coordinates and will vary depending on the number of equations (degrees of freedom) needed to fully represent the system. D is related to the Rayleigh dissipation energies and Fe is the external force, if any.

The Equation (3.7) presents the kinetics energy from the system shown in Figure 17.

$$E_k = \frac{1}{2}M\dot{x}^2 + \frac{1}{2}J\dot{\varphi}^2 + \frac{m}{2}\left(\dot{X}^2 + \dot{Y}^2\right) \tag{3.7}$$

where M is the sum of the electromechanical system mass with the mass of unbalance. The displacement of the mass is given by x.

In the Equation (3.7), $\dot{X}$ and $\dot{Y}$ are used as a new point of reference to locate the unbalanced mass in the Cartesian plane.

The potential energy of the non-ideal system in study is given by Equation (3.8).

$$E_p = \frac{1}{2}kx^2 \tag{3.8}$$

where k is the stiffness of the system spring element. The dissipative forces are given by Equation (3.9).

$$D = \frac{1}{2}c\dot{x}^2 \tag{3.9}$$

where c is the viscous damping coefficient of the mechanical structure.

Substituting the Equations (3.5) into the Equation (3.6) and deriving this resultant equation with respect to the generalized coordinates, one obtains the complete set of equations that represents the non-ideal system in the study, shown in Equation (3.10).

$$(M + m)\ddot{x} + c\dot{x} + kx - mr\left(\dot{\varphi}^2\sin\varphi + \ddot{\varphi}\cos\varphi\right) = 0$$
$$\left(J + mr^2\right)\ddot{\varphi} + mr\ddot{x}\cos\varphi = S(\dot{\varphi}) \tag{3.10}$$

where $S(\dot{\varphi})$ is the motor's net torque function. However, the objective of this work is to obtain a complete non-ideal model. Thus, it is necessary an equation that relates the torque generated by the motor with the applied voltage in the armature, serving them as a control parameter of the system. To find this equation, we started with the deduction of the basic equations that define the behavior of a direct current electric motor.

The electric motor is an electromechanical component that transforms electrical energy into mechanical energy through the rotation of its axis. In a permanent magnet type motor, the electric field is generated by a constant magnetic flux that arises through the use of magnets, where the voltage applied in the armature is the component that controls the angular velocity of the shaft. Figure 18 shows a schematic of a permanent magnet type DC motor, where R is the armature resistance, L is the armature inductance, i_{mtr} is the electric current through the motor and T_{mtr} is the torque generated (NISE; DA SILVA, 2002).

The torque generated by the motor is proportional to the current passing through the armature, thus:

$$T_{mtr} = K_T i_{mtr} \tag{3.11}$$

where K_T is a constant of proportionality named torque constant.

Figure 18 - Electric Motor Schematics
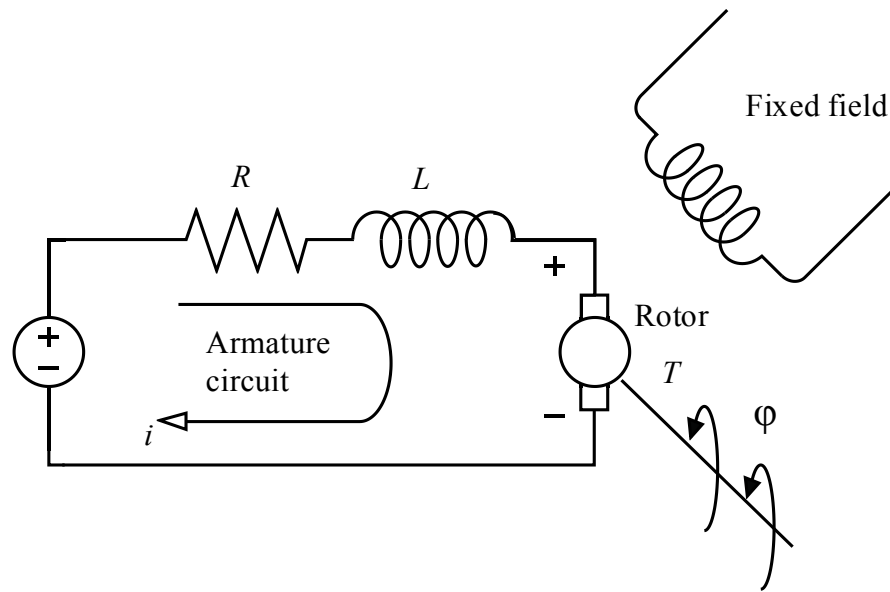
The Counter-Electromotive Force (CEMF) arises in the armature when the motor is running. This value can be represented by the product of the angular velocity with the magnetic flux, as shown in the Equation (3.12).

$$V_{CEMF} = K_B \varphi \tag{3.12}$$

where K_B is a constant of proportionality called counter-electromotive force constant (NISE; DA SILVA, 2002).

Since the electric motor consists of an electromechanical system, two equations are required to represent its behavior: an equation related to the mechanical part, and another equation related to the electrical part.

Through the use of Newton's second law, the mechanical equation of the system under study can be defined as:

$$J\ddot{\varphi} + b\dot{\varphi} = K_T i_{mtr} \tag{3.13}$$

where b is the viscous friction of the mechanical parts of the motor, i_{mtr} is the current that passes through the armature and J is the moment of inertia from all the mechanical parts of the motor system.

For the electric equation, the Kirchhoff's Voltage Law can be used in the circuit shown in Figure 18, obtaining:

$$L\frac{di}{dt} + R_{mtr} i_{mtr} = V_{mtr} - K_B \dot{\varphi} \tag{3.14}$$

The Equations (3.13) and (3.14) together represent the complete system of a DC electric motor, where the voltage parameter (V_{mtr}) controls the angular velocity ($\dot{\varphi}$) of the motor shaft.

By making the coupling and adjustments, the set of Equations (3.10) can be rewritten in the form presented by the Equation (3.15).

$$M\ddot{x} + c\dot{x} + kx - mr\left(\dot{\varphi}^2 \sin\varphi + \ddot{\varphi}\cos\varphi\right) = 0$$

$$\left(J + mr^2\right)\ddot{\varphi} + mr\ddot{x}\cos\varphi = K_T i_{mtr} - b\dot{\varphi} \qquad (3.15)$$

$$\frac{di}{dt} = \frac{-R_{mtr}i_{mtr} + V_{mtr} - K_B\dot{\varphi}}{L}$$

The set of Equations (3.15) represents the non-ideal system shown in Figure 17, where the mechanical equations are coupled with a full DC motor equation. The voltage V is the motor speed control parameter, in this case also being responsible for the mechanical system vibration due to the unbalanced mass m.

4.3 NUMERICAL SIMULATIONS

Numerical simulations are fundamental tools in the design of new systems, projects or products. They allow predicting the behavior of the system, reducing the number of prototypes required and the time consumed in their constructions. All the constitutive equations presented in this work consist of Ordinary Differential Equations (ODE). In this kind of equations, there is an unknown function (the solution(s)) and its derivatives. The purpose of this chapter is to show the behavior of the system over time. For this objective, it was decided to use a numerical iterative integrator. The proposed method is the Runje-Kutta of 4ºorder, also known as the RK4 method.

4.3.1 Numerical Integration

The implementation of the RK4 method requires the knowledge of the system and his initial conditions. Choosing a step size greater than zero ($h > 0$), the approximation of the function y at $t+1$ is given by:

$$y_{n+1} = y_n + \frac{1}{6}(k_1 + 2k_2 + 2k_3 + k_4)$$

$$t_{n+1} = t_n + h$$

(3.16)

where k_{1-4} are four different increments shown in the sequence.

$$k_1 = hf\left(t_{(i)}, y_{(i)}\right)$$

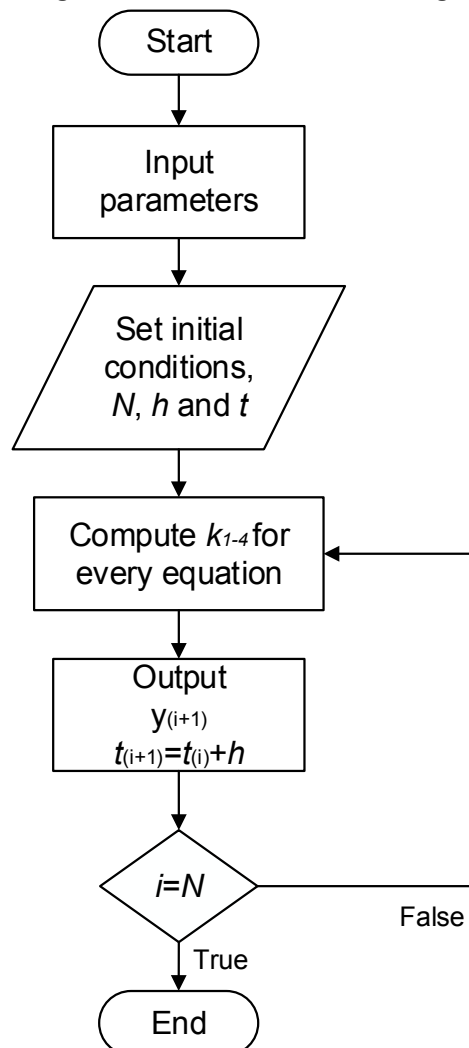$$k_2 = hf\left(t_{(i)} + \frac{h}{2}, y_{(i)} + \frac{k_1}{2}\right)$$

$$k_3 = hf\left(t_{(i)} + \frac{h}{2}, y_{(i)} + \frac{k_2}{2}\right)$$

$$k_4 = hf\left(t_{(i)} + h, y_{(i)} + k_3\right)$$

(3.17)

The algorithm of the integrator was developed following the flowchart is shown in Figure 19, where N is the number of iterations.

Figure 19 - Flowchart of the Integrator Used

Source: Self-Authorship

4.3.2 Numerical Simulation of the Non-Ideal System

The objective of this subsection is to simulate the non-ideal system given by the Equation (3.15) seeking to obtain its non-ideal behavior. This system of equations can be put in the following form:

$$\ddot{x} = \frac{-c\dot{x} - kx + mr\left(\dot{\varphi}^2 \sin\varphi + \ddot{\varphi}\cos\varphi\right)}{M}$$

$$\ddot{\varphi} = \frac{K_T i_{mtr} - b\dot{\varphi} + mr\ddot{x}\cos\varphi}{J + mr^2} \qquad (3.18)$$

$$\frac{di_{mtr}}{dt} = \frac{V_{mtr} - K_B\dot{\varphi} - R_{mtr}i_{mtr}}{L}$$

Initially, the equations of the system need to be reduced to first order differential equations. The following substitutions are made: $x_1 = x$; $x_2 = \dot{x}$; $\dot{x}_2 = \ddot{x}$; $x_3 = \varphi$; $x_4 = \dot{\varphi}$; $\dot{x}_4 = \ddot{\varphi}$; $x_5 = i_{mtr}$; $\dot{x}_5 = \dfrac{di_{mtr}}{dt}$ and $u = V_{mtr}$. Furthermore, the set of equations for the non-ideal system is rewritten in the following form:

$$\dot{x}_1 = x_2$$

$$\dot{x}_2 = -\frac{cx_2}{M} - \frac{kx_1}{M} + \frac{mr\left(x_4^2 \sin x_3 + \dot{x}_4 \cos x_3\right)}{M}$$

$$\dot{x}_3 = x_4 \qquad (3.19)$$

$$\dot{x}_4 = \frac{K_T x_5}{J + mr^2} - \frac{bx_4}{J + mr^2} + \frac{mr\dot{x}_2 \cos x_3}{J + mr^2}$$

$$\dot{x}_5 = \frac{u}{L} - \frac{K_B x_4}{L} - \frac{Rx_5}{L}$$

Before the simulations were performed, the system needed to have its equations reduced and decoupled so that only one second derivative with respect to time is present in each equation.

Table 3 presents the parameters used in the numerical simulations, where all the processes of obtaining these parameters are described in Appendices A and B.

The initial conditions used are: $x_1(0) = 0$, $x_2(0) = 0$, $x_3(0) = 0$, $x_4(0) = 0$, $x_5(0) = 0$.

Table 3 - Properties of the Non-Ideal System

Parameter	Value	Unit
k	541	N/m
c	0.07	$N.s/m$
M	0.250	kg
m	0.012	kg
K_T	0.0211	$N.m/A$
K_B	0.0211	$V.s/rad$
J	0.82×10^{-4}	$kg.m^2$
L	3.1×10^{-3}	H
b	8.17×10^{-7}	$N.m.s/rad$
r	0.02	m
R	41	Ω

Source: Self-Authorship

Figure 20 shows the variation in the motor's angular frequency and the vibration amplitudes.

Figure 20 - Jump Effect Considering the Angular Frequency of the Motor
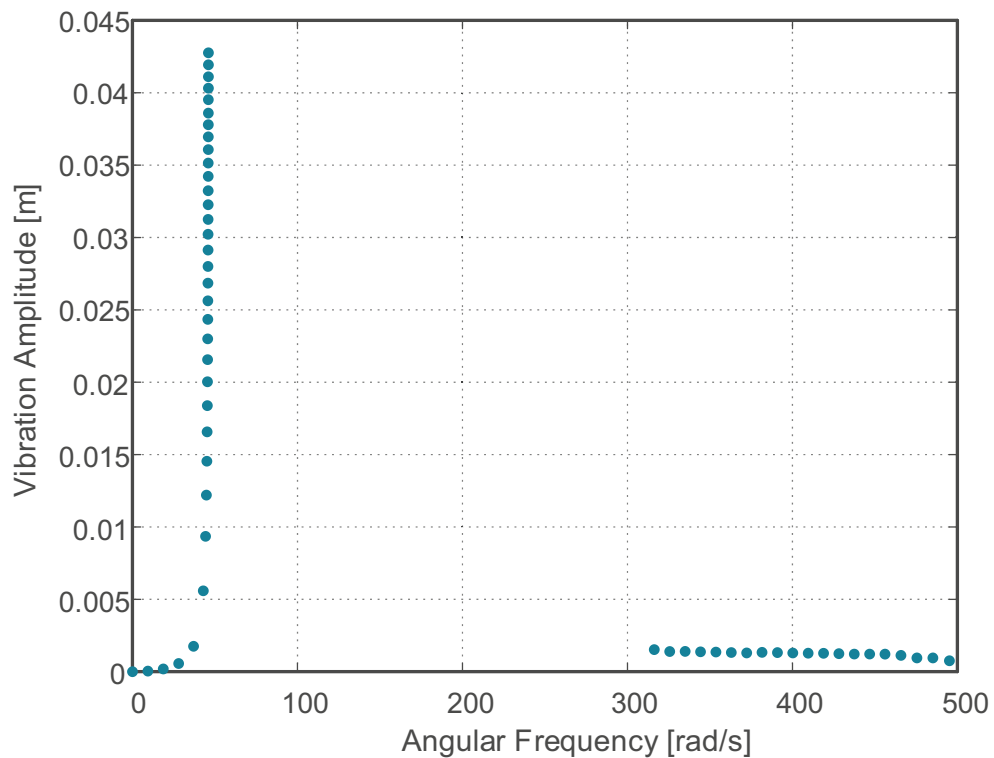
Source: Self-Authorship

Figure 21 shows the variation of the vibration amplitudes through the increase of the motor's voltage. As can be seen, the jump occurred in the voltage value of 6.6 volts.

Figure 21 - Jump Effect Considering the Voltage Applied in the Motor

Source: Self-Authorship

Figure 22 presents the relation of the angular frequency with the applied electric voltage in the DC motor. The horizontal sequences in Figure 22 show that even increasing the electric voltage, the angular frequency (motor rotation) does not change their values at all, and this energy only increases the vibration of the system.
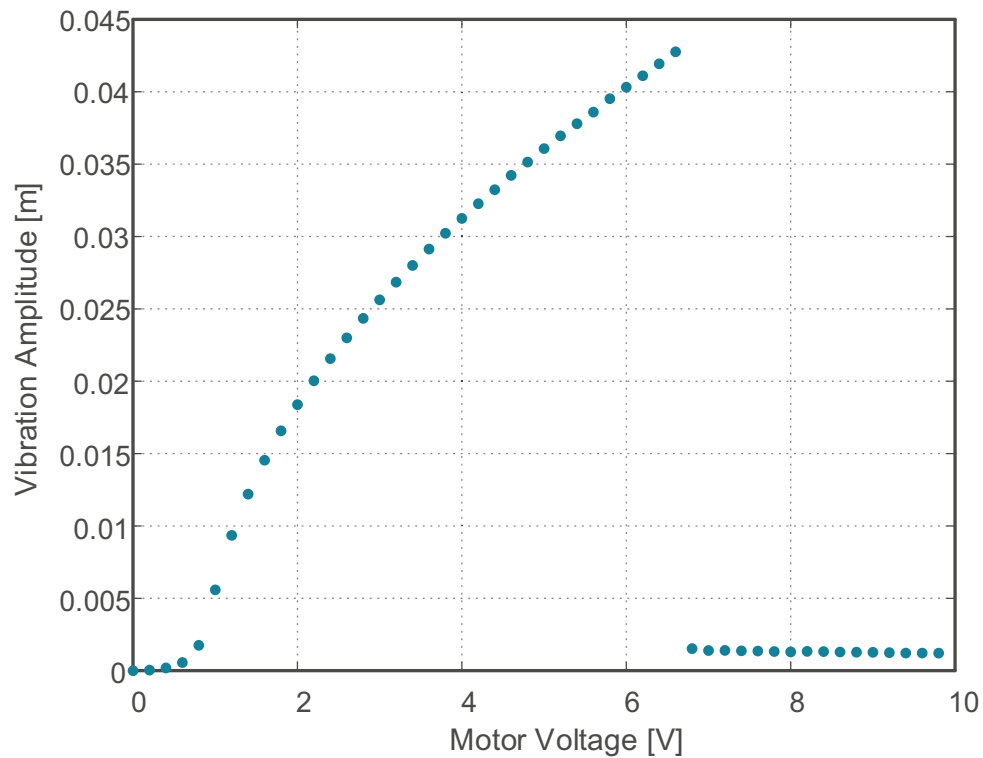
The obtained mathematical model can demonstrate the non-ideal behavior and the Sommerfeld effect as expected. However, through Figure 21 it is also possible to observe that the Sommerfeld effect occurs in a relatively low motor voltage. This occurs because the chosen motor has a high nominal speed and the mechanical structure has a low natural frequency. This result in a low electrical voltage required to rotate the axis at the same frequency as the natural frequency of the entire system.

Figure 22 - Relation between the Voltage Applied and the Angular Frequency
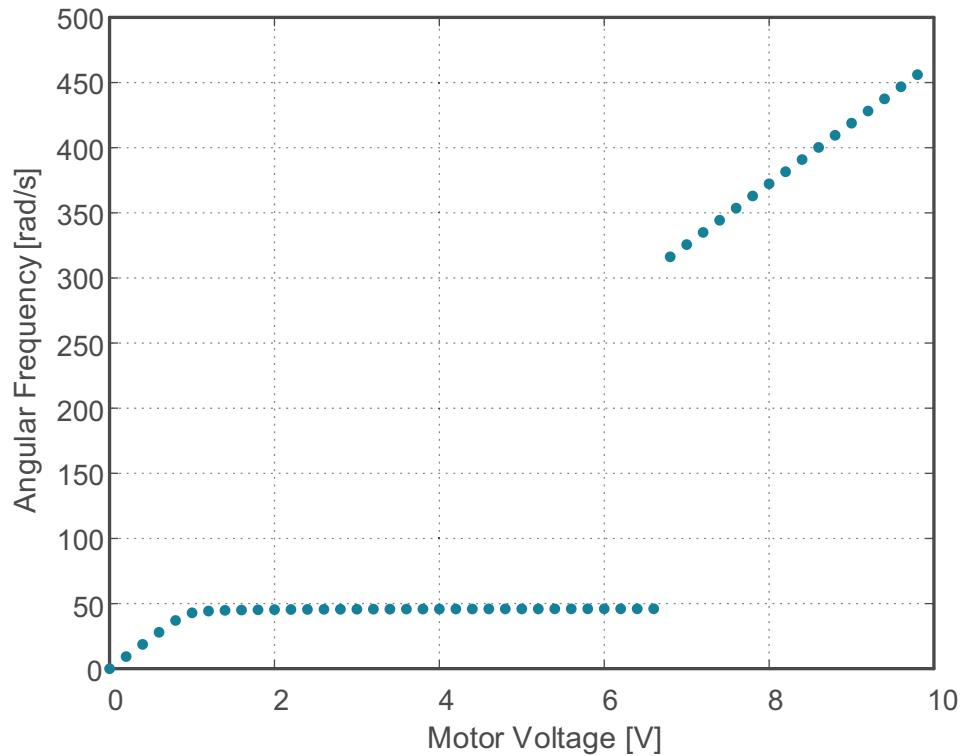
Source: Self-Authorship

4.4 SUMMARY

Numerical simulations constitute one of the main tools in the design of new machines and systems. This tool is common and widely used in dynamical systems analysis.

For a non-ideal type system, the constitutive model must consider the coupling of the mechanical part with the electrical part. To obtain the model of the system in the study, it was necessary to start from the basic equations for both the mechanical structure and the DC electric motor. The model obtained considers the mechanical system as a 2DOF system composed of a mass and a rotating axis, where the axis velocity is controlled by the voltage applied in the electric motor. As the axis turns, his unbalance causes the system to vibrate. For the numerical simulations, a Runje-Kutta of fourth order algorithm was written and simulated through the use of real system parameters, which were previously validated and shown in the Appendixes of this thesis.

5 EXPERIMENTAL SYSTEM AND RESULTS

This chapter aims to present the construction, instrumentation and tests results for the experimental model of the non-ideal type system studied in this thesis. A non-ideal system consisting of an aluminum beam and an electric DC motor was built. The beam is fixed at one of its ends, where the other is free to vibrate (cantilever beam). An unbalanced electric motor is used as a non-ideal energy source. Tests were done aiming to capture the non-ideal behavior of the system, thus obtaining the vibration amplitudes and the speed of the motor during the process. This chapter also presents the final results of this master's thesis, showing comparative results of the vibration control for the proposed SMA actuator.

5.1 EXPERIMENTAL SET-UP

The prototype of the system consists of a flat cantilever beam. At the free end of the beam, an unbalanced Direct Current (DC) motor is attached. For unbalance, a small standard weight is attached to the motor shaft. Because of the motor imbalance, the mechanical structure will present a vibratory behavior when the system comes into operation. Figure 23 shows the described system.

Figure 23 - Experimental Non-ideal System Built
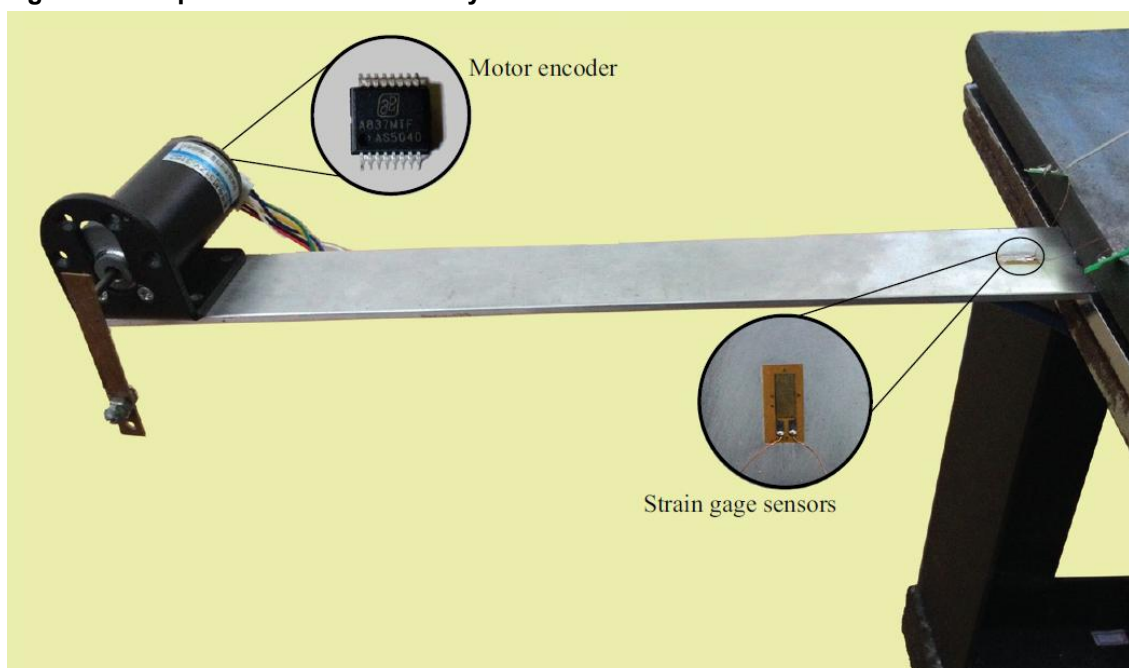
Source: Self-Authorship

Table 4 shows the physical parameters from the mechanical structure used.

Table 4 - Properties of the Mechanical Structure

Parameter	Value	Unit
Density	2700	kg/m^3
Young's Modulus	$69x10^9$	Pa
Length	0.32	m
Width	0.038	m
Height	0.003	m

Source: Self-Authorship

An instrumentation system was built with the purpose of obtaining the data structure vibration and the rotation of the motor. This system is described in the sequence.

5.1.1 Instrumentation System

The first objective of the instrumentation system when studying a vibratory system is to acquire the behavior of the structure over the time. For this objective, in this thesis were used strain gage type sensors. This type of sensor has an extremely low mass, not physically influencing the system. Another advantage of this kind of sensor is the possibility to make measurements both of static and dynamic systems.

The principle of operation of a strain gage is a relation between the variations of its electrical resistance through the variation of its physical dimensions, i.e., transforming the deformation into an electrical quantity that can be measured. Basically, when the structure undergoes a tensile stress, the geometric section of the extensometer will suffer a reduction and the electrical resistance will suffer an increase. Similarly, when a compressive stress is applied, the section of the strain gage will increase and consequently the electric resistance will be reduced. This difference of resistances can then be used to relate the deformation that the material is suffering.

A Wheatstone bridge was used to read the strain gage sensor, this being a common circuit used to discover the value of an unknown electrical resistance. This circuit may have different configurations based on the number of strain gauges used; the option chosen for this work is the half-bridge circuit, with two active strain gauges

and two defined resistors. This configuration eliminates the effects of temperature and causes the output signal to be doubled. Figure 24 shows the configuration of the half-bridge sensors in the mechanical system.
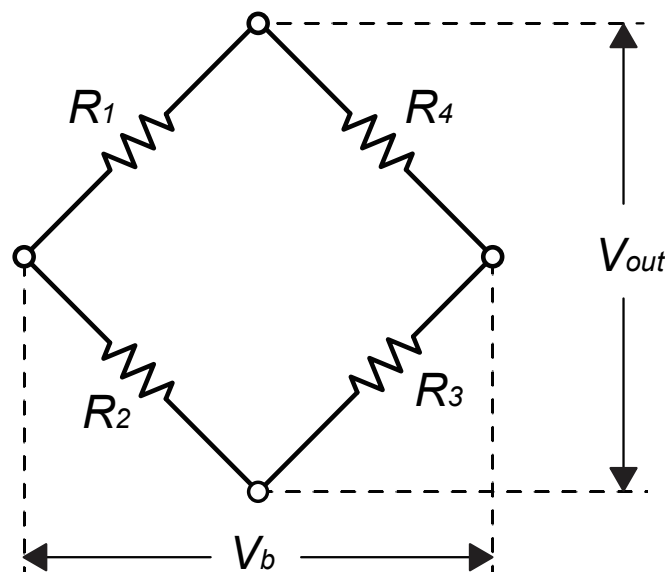
Figure 24 - Positioning of the Strain Gage
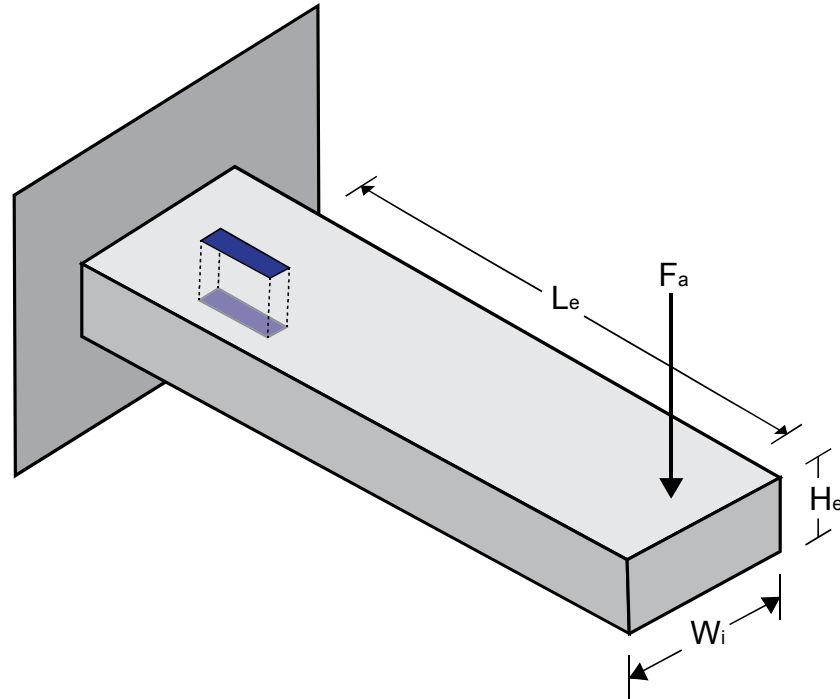
Source: Self-Authorship

Figure 25 shows a characteristic Wheatstone bridge circuit used to relate the deformation suffered by the strain gage and the structure.

Figure 25 - Wheatstone Bridge

Source: Self-Authorship

Considering the Figure 25 as a ½ (half) bridge, the resistors R_1 - R_2 are the strain gauges used for the measurements and R_3 - R_4 are fixed resistors. The bridge is considered in balance when all the components have the same electrical resistance. Equation (4.1) relates the stress applied to the bridge with the deformation suffered by the strain gauge.

$$\frac{V_{out}}{V_b} = \frac{k_{sg}\eta}{2} \tag{4.1}$$

where V_{out} is the output voltage of the bridge (the signal to be amplified), V_b is the bridge voltage, k_{sg} is the strain gage factor and η is the deformation suffered by the strain gage.

The deformation of both the strain gage shown in Figure 24 is given by Equation (4.2).

$$\eta = \frac{6F_a L_e}{E_b W_i H_e^2} \tag{4.2}$$

The signal generated by the strain gage sensor through the Wheatstone bridge has a very low magnitude scale. Thus, it is necessary to amplify the signal before sending it to the acquisition system. Commonly, an operational amplifier could be used for this purpose. In this thesis, the integrated circuit INA129 from Texas Instruments was used for this purpose. This CI has high precision and low consumption. Their gain value can range from 1 to 10.000 depending only on one resistor installed.

The amplification gain of the INA129 circuit is given by Equation (4.3).

$$G = 1 + \frac{49.9k\Omega}{R_G} \tag{4.3}$$

where G is the gain and R_G is a resistor with a stipulated value according to the level of amplification that is desired to obtain.

Figure 26 shows the circuit built to amplify the signal that comes from the extensometer and to send it to the acquisition system. Figure 26a shows the schematic circuit and Figure 26b shows the circuit built, where this circuit also contemplates the Wheatstone bridge.

Figure 26 - Amplification Circuit

<div align="center">a)   b)</div>
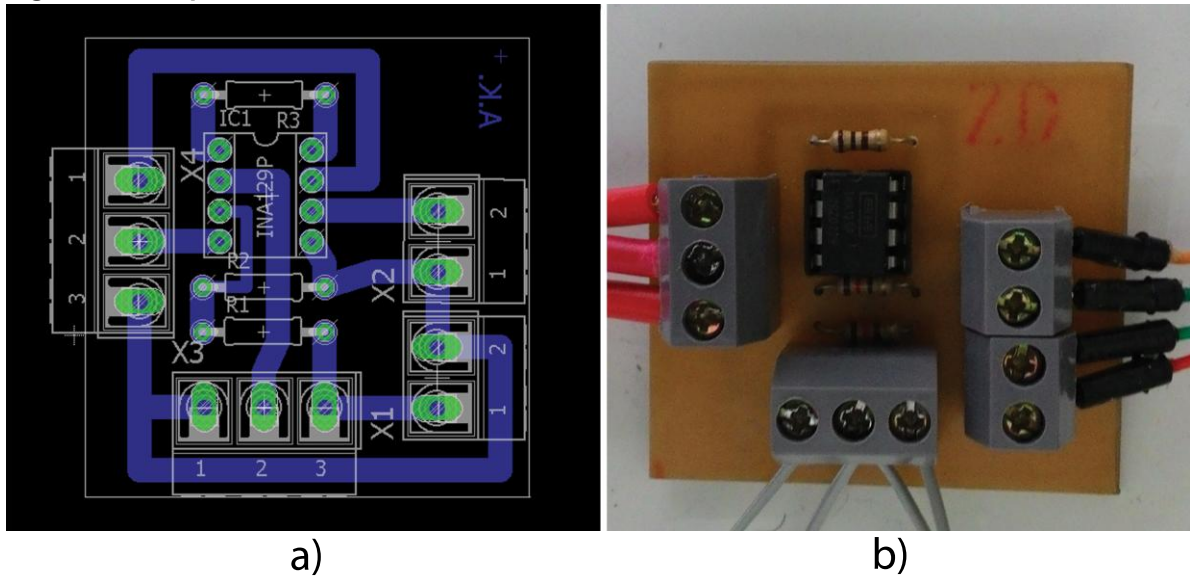
Source: Self-Authorship

5.1.2 Natural Frequency of the Non-Ideal System

A parameter of great importance when analyzing a vibratory system is its natural frequency. The natural frequency of a system is defined as the frequency at which the system continues to vibrate after being excited by a transient initial disturbance, where an external excitation at this specific frequency can drive the system to oscillate at greater amplitudes (RAO; YAP, 2011; SHIGLEY, 2011). In the designing process of a system or machine, the natural frequencies must be known in order to prevent the system to operate in these ranges, as this can cause structural and operational problems. In this thesis, it is considered that the non-ideal system will pass through its region of resonance, something necessary for the Sommerfeld Effect to appear. Thus, for the SMA material to act correctly, the natural frequency near the resonance region where the jump occurs must be known.

Several methods can be used to find the natural frequencies of a dynamic system. Among these methods, we have analytical methods, where the dynamic equations of the system are necessary; experimental methods, when the system has already been built or numerical methods, where some CAE (Computer-Aided Engineering) software is commonly employed.

To obtain the natural frequency in an experimental way, the system can be excited in some way (e.g., releasing the system from a basic initial condition) and then its vibration frequencies can be analyzed to determine the most impacting

frequency occurring. Figure 27 shows an experimental acquisition of the free vibration over the time for the studied system. For this result, the tip of the beam was released from a determined initial condition that, in this case, was equal to the deformation caused by a force of 4,9N.

Figure 27 - Free Vibration of the Prototype Built
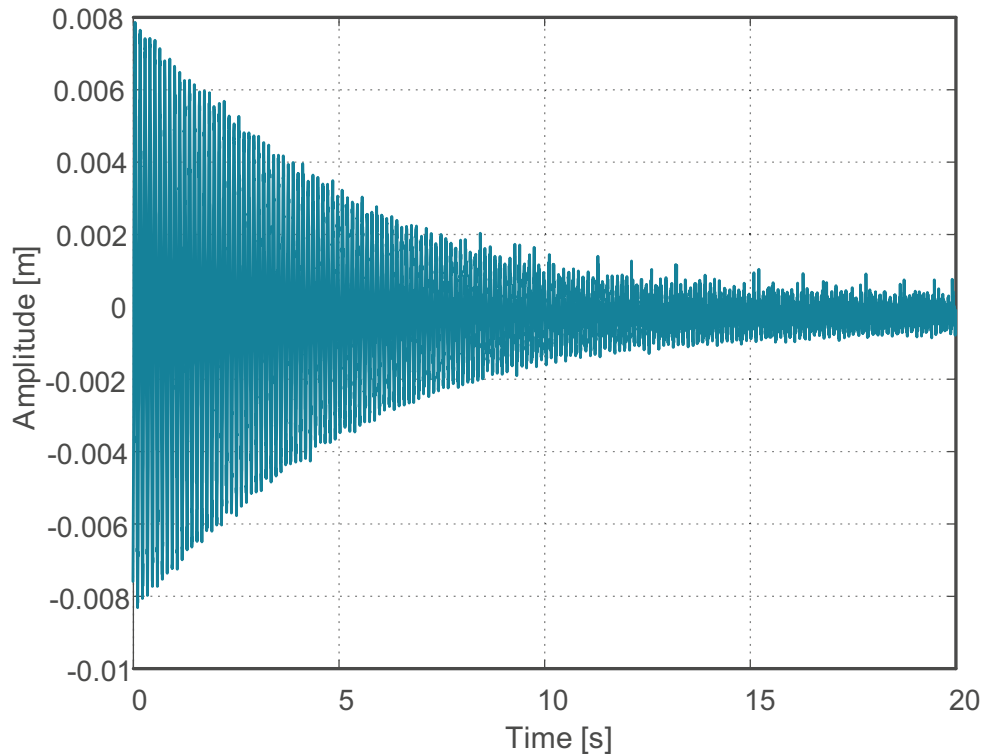
Figure 28 shows the main frequencies present in the system, this result is obtained through the use of a Fast Fourier Transform (FFT). Clearly, it is perceived that one frequency stands out over the others; this is the natural frequency of the system in this vibration mode (fundamental mode).

Analytically, the natural frequency of the first vibration mode of the mechanical system can be obtained through the Equation (4.4).

$$f_n = \frac{1}{2\pi}\sqrt{\frac{k}{M}} \tag{4.4}$$

where k is the stiffness constant of the structure and M is the total mass (APPENDIX A).

Using the Equation (4.4) and the parameters from the mechanical system present in Appendix A, it is possible to find a natural frequency equivalent to 8.42 *Hz*.

Figure 28 - Frequencies of the System
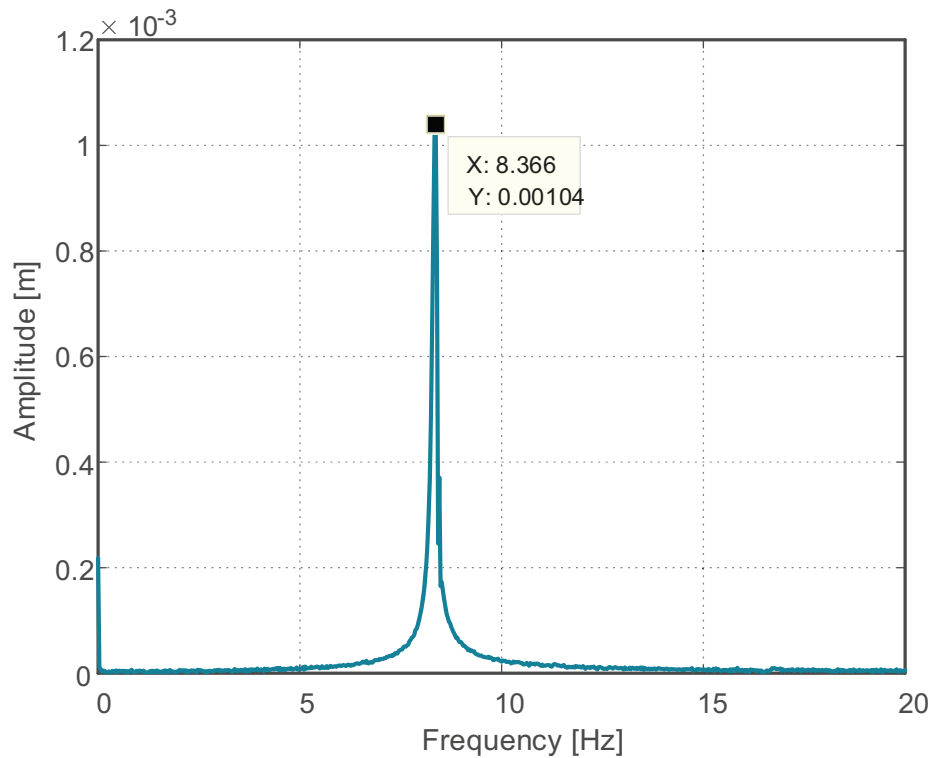
Source: Self-Authorship

Comparing the natural frequency value obtained experimentally (8.36 *Hz*) and the value obtained in an analytical way (8.42 *Hz*), we can see a great similarity between the two values, showing that the parameters of the mechanical system obtained are correct and show a great correlation with the real system.

5.1.3 Experimental Behavior of the Non-Ideal System Built

Figure 29 shows the experimental behavior of the system considering the jump phenomenon.

The behavior of the jump structure occurring in Figure 29 of the experimental system presents slight differences when compared to the results of the numerical simulations from the Chapter 4. It is noticed that the system has a slight increase of angular velocity in the region of the jump in the experimental system. In the numerical system, this increase does not exist, where the system maintains the same angular velocity during almost all the period before the jump. The angular frequency where the jump effect occurs also shows a slight difference when compared to the numerical system. In the experimental results, the jump occurs in a lower angular frequency or a lower motor speed. However, considering the point of occurrence of

the jump and all the values, it's realized that this experimental result shows a great similarity with the numerical system previously showed in Chapter 4.

Figure 29 - Jump Effect Considering the Angular Frequency of the Motor
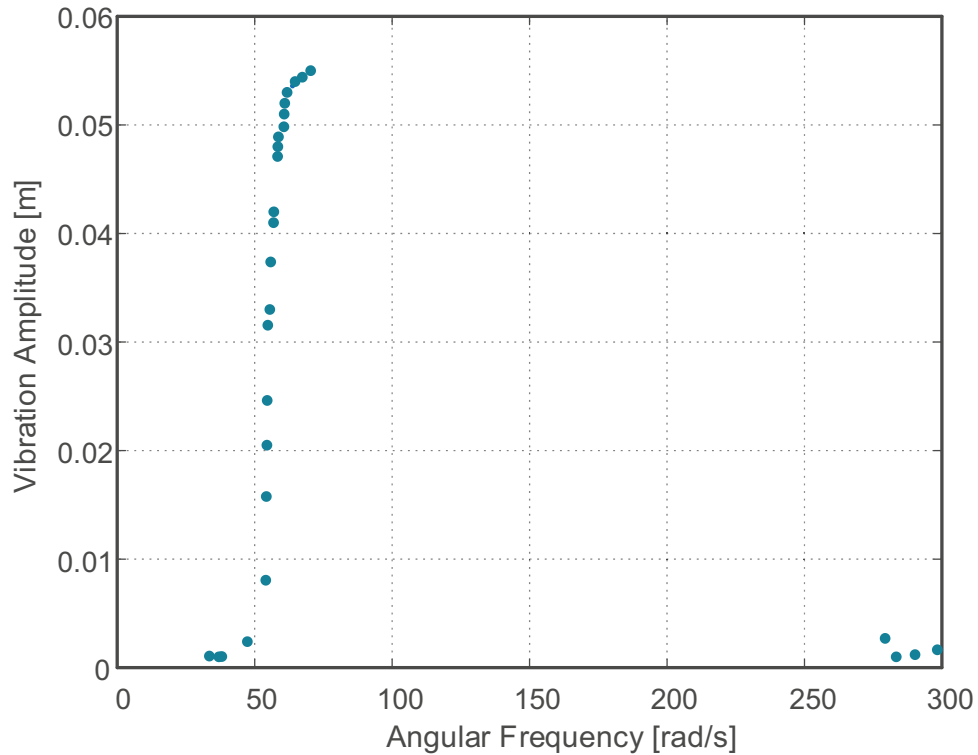
Figure 30 presents the Sommerfeld effect based on the electric voltage applied to the electric motor. Again, it is possible to observe a great similarity of these results with the numerically simulated system, where the jump occurred in the voltage value of 6.2 volts versus the 6.6 volts of occurrence in the numerical system. This difference can be caused by considerations made to obtain the mathematical model, such as the resistance of the air that has been disregarded, or the consideration of the mechanical system being a lumped-parameter system, with the structural parameters of the system (mass, stiffness, and damping) being concentrated in one point. Probably, a mathematical model conceived through the continuous mechanics or Finite Elements Analysis (FEM) could present even a better result when compared to the real system.

Figure 30 - Jump Effect Considering the Voltage Applied in the Motor
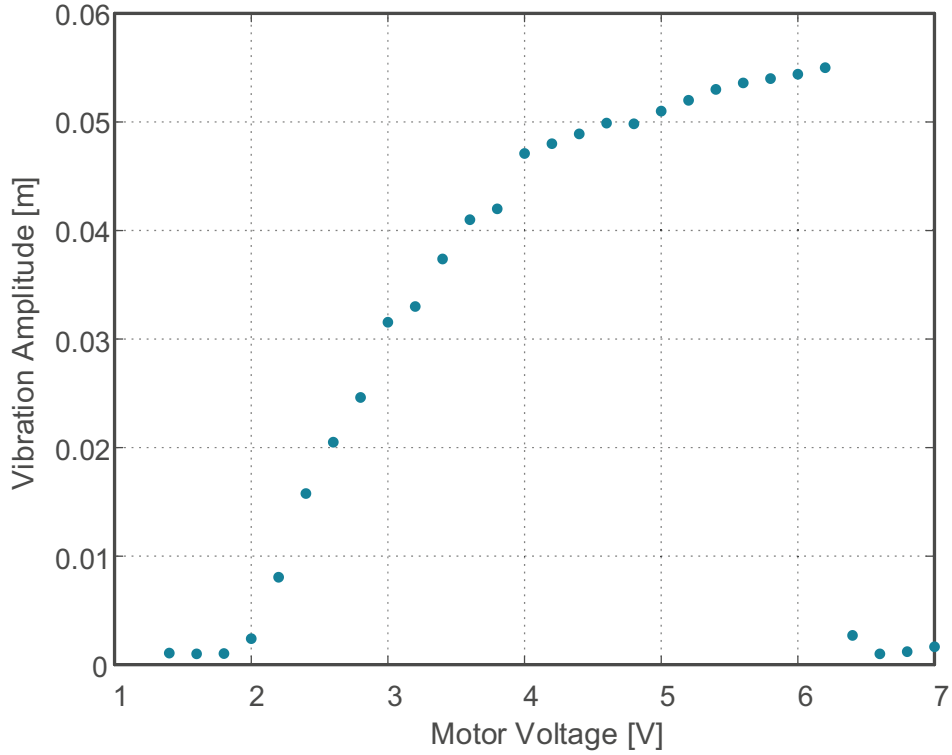
Figure 31 shows the relation between the angular frequency and the voltage applied to the motor.

Figure 31 - Relation between the Angular Frequency and the Motor Voltage

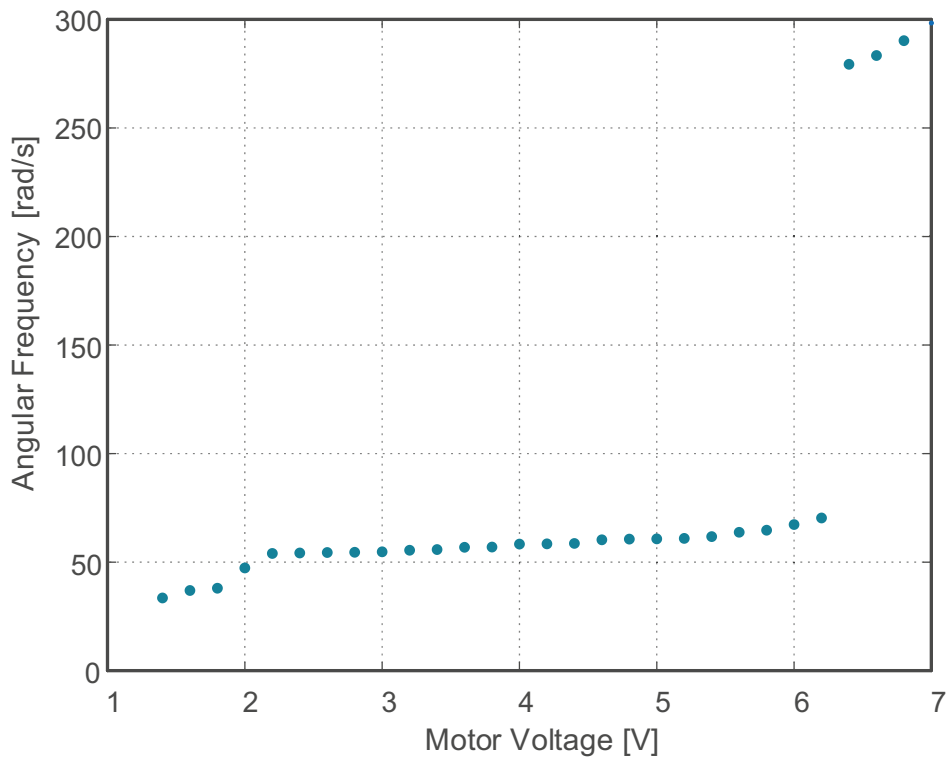As explained in Chapter 4, this type of graph has the objective to show the loss of energy, normal to the non-ideal systems. All horizontal sequence of points shows a stagnation of the angular frequency even though there is an increase in the motor voltage. This means that the motor is not responding to the voltage increase in a linear way as expected.

All these results presented in this section are very similar to the results of the numerical system, previously shown in chapter 4. The systems showed the jump effect at a very similar electrical voltage. It is also emphasized, even with the parameters and simulations of the mechanical system and the electrical system showing enormous correlations with the real behaviors, when using the model presented by the set of Equations (3.16) there is a slight difference in the non-ideal effects expected (jump phenomenon) when compared to the real system.

5.2 ATTENUATION OF THE SOMMERFELD EFFECT

The practical implementation of the SMA actuator is the final objective of this thesis. In the following sections are presented the proposed control of the non-ideal behavior of the system and the experimental results obtained.

5.2.1 Proposed Control

In this part of the thesis is proposed the control of the system's non-ideal behavior with the implementation of an SMA actuator in an experimental approach. The non-ideal system built was previously described, now, an SMA actuator similarly of the one used in Chapter 3 is implemented physically in the non-ideal system. The SMA material has one of his ends fixed and another attached in the tip of the non-ideal system, the same point where the vibrations signal if acquired. Through force decomposition, it is noticed that when the actuator is installed parallel to the structure, the force generated by the SMA material is derisory, not affecting the system. Thus, a minimum angle is necessary. It was decided to install the actuator considering a small angle of 15 degrees with the mechanical structure. This angle showed a great set of results at the same time that it doesn't change too much the

geometry of the system. Figure 32 shows the installation schematics for the proposed SMA actuator in the non-ideal system.

Figure 32 - Non-Ideal System with the SMA Actuator
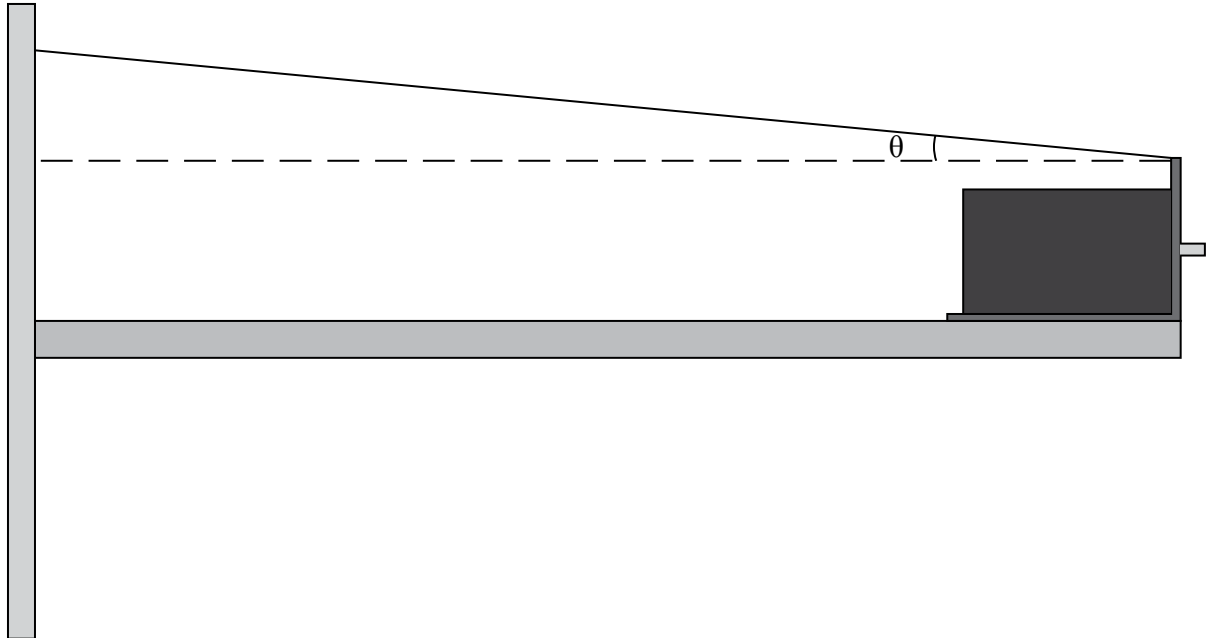
Source: Self-Authorship

Only the strain energy generated by the SMA material is considered on the structure-actuator coupling. Thus, are disregarded all types of influences caused by the actuator mass or geometry (e.g., inertia, weight force and air resistance).

When the actuator is heated, the material suffers a physical contraction and consequently generates a force in the system. This force will be used to hold down the system, making it not vibrate.

For the actuation of the SMA material, an ON/OFF controller is projected. This controller activates the actuator when the vibration frequency of the system comes to a predefined value below the natural frequency, the point of occurrence of the Sommerfeld effect. In this case, for a better performance, the controller was programmed to act in a frequency of 3Hz. this value was chosen due to the rapid increase in the system frequency in the tests. This occurs because the system presented a low electrical voltage necessary for the occurrence of the jump. Thus, is possible to observe that the controller begins to act a brief moment after starting the operation of the system.

When the vibration amplitudes of the system decrease, the controller turns off the actuator shutting off his energy. Figure 33 shows a block diagram of the system proposed.

Figure 33 - Block Diagram of the Proposed Control
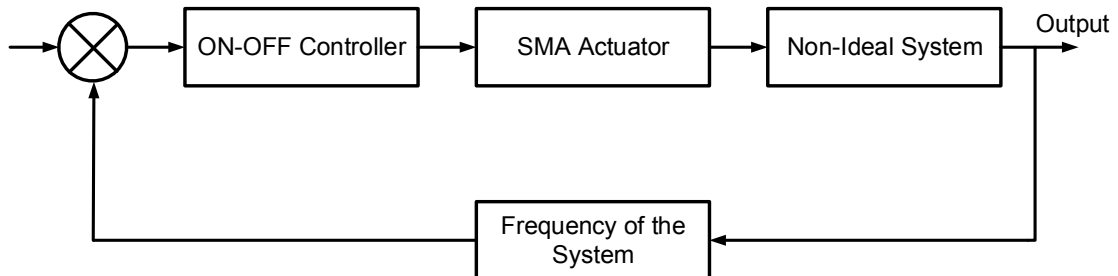
Source: Self-Authorship

For the tests performed, the motor voltage is continuously increased with a pre-set value of voltage per time. This allows the system to go through the jump region and continue working. After the motor reaches the final voltage, which for tests is 14 *volts*, the whole system shuts off, and the test is finalized.

The next section presents the experimental results of the tests performed.

5.2.2 Experimental Results

Figure 34 shows the behavior of the system without the implementation of the SMA actuator and the ON/OFF control. To obtain this type of graph, and the similar ones, a PWM (Pulse Width Modulation) was implemented through a microcontroller. The PWM allowed the motor voltage to increase as time went by, passing the system through the resonance region and thus, obtaining the Sommerfeld effect from the system.

In Figure 34 it is possible to observe that the system reaches a peak of vibration with an amplitude of approximately 0.052 meters, with the Sommerfeld effect (jump phenomenon) occurring approximately at 6.38 volts. It is noticed that after the jump effect occurrence, the vibration amplitudes fall abruptly, remaining considerably unchanged, even when we have the increase of the motor voltage to higher values. As it can be observed, the motor starts its operation from 1 volt, this being the minimum voltage to break the inertia of the mechanical parts of the system.

Figure 34 - Behavior of the System without SMA
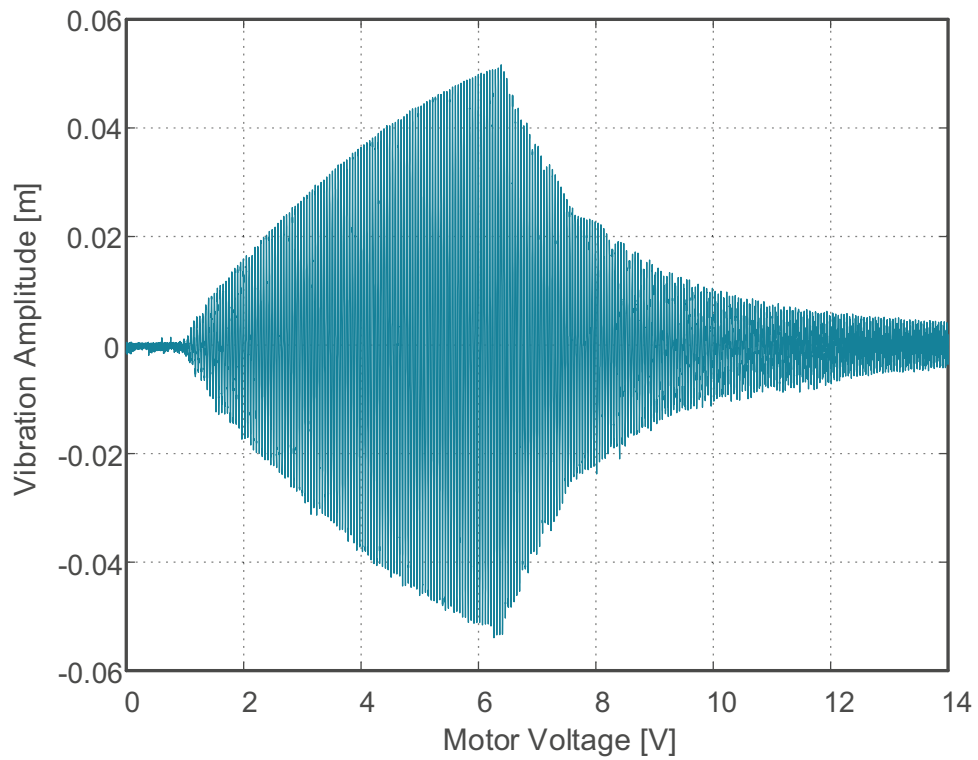
Figure 35 shows the electric current consumed by the motor during the test.

Figure 35 - Electric Current used by the Motor
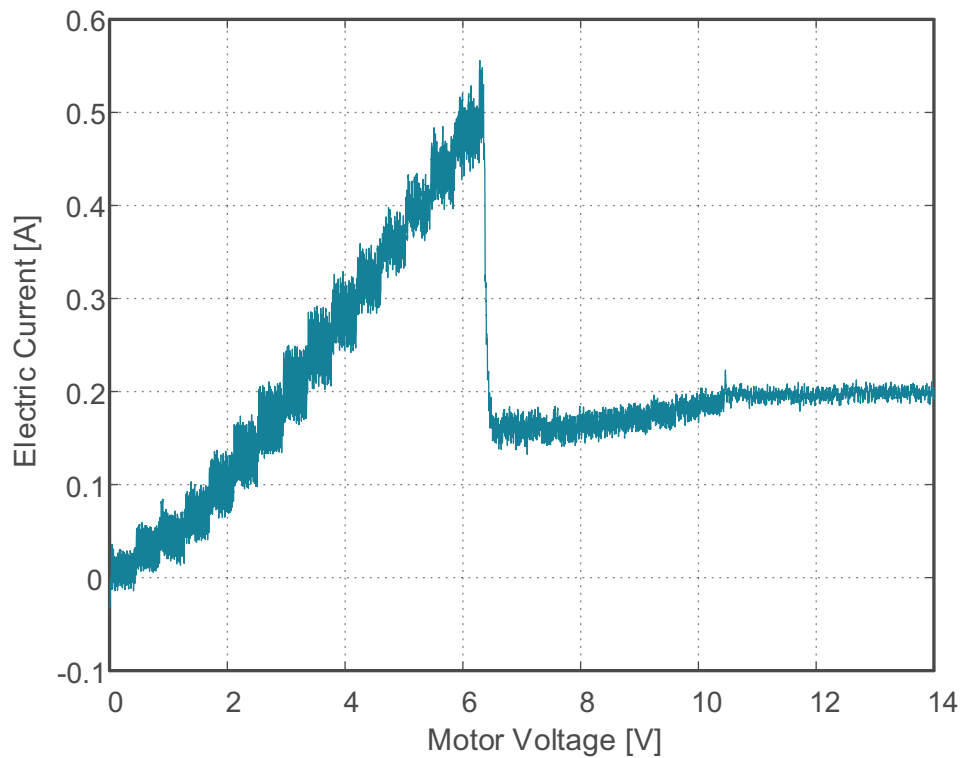
As can be seen, the jump effect also occurs in the current consumed by the motor. As the amplitudes of vibration increase, the current consumed by the motor tends to increase proportionally, even with the angular frequency of the motor not increasing at all. This effect was little explored in the literature, being an effect of great impact for the electric motor because of the occurrence of current values higher than the nominal ones, also causing a greater loss of energy and badly impacting in the power supply of the entire system.

It is possible to observe that the current peak also coincides with the voltage value where the Sommerfeld effect occurs. This shows that when the Sommerfeld effect occurs, not only the voltage applied is loosed, but the electric current consume is also abnormally increased at the same point.

Figure 36 presents the behavior of the motor speed during the test. As can be seen, when the system starts to vibrate the speed of the motor stops to increase. Because of this effect, is possible to see an almost horizontal region in the graphic, where the motor speed value does not change with the increase of the voltage. After the passage of the Sommerfeld effect, the motor responds to the increased voltage, and it is possible to observe the normal correlation between the increase of voltage and the increase of the motor speed.

Figure 36 - Motor Speed during the Sommerfeld Effect
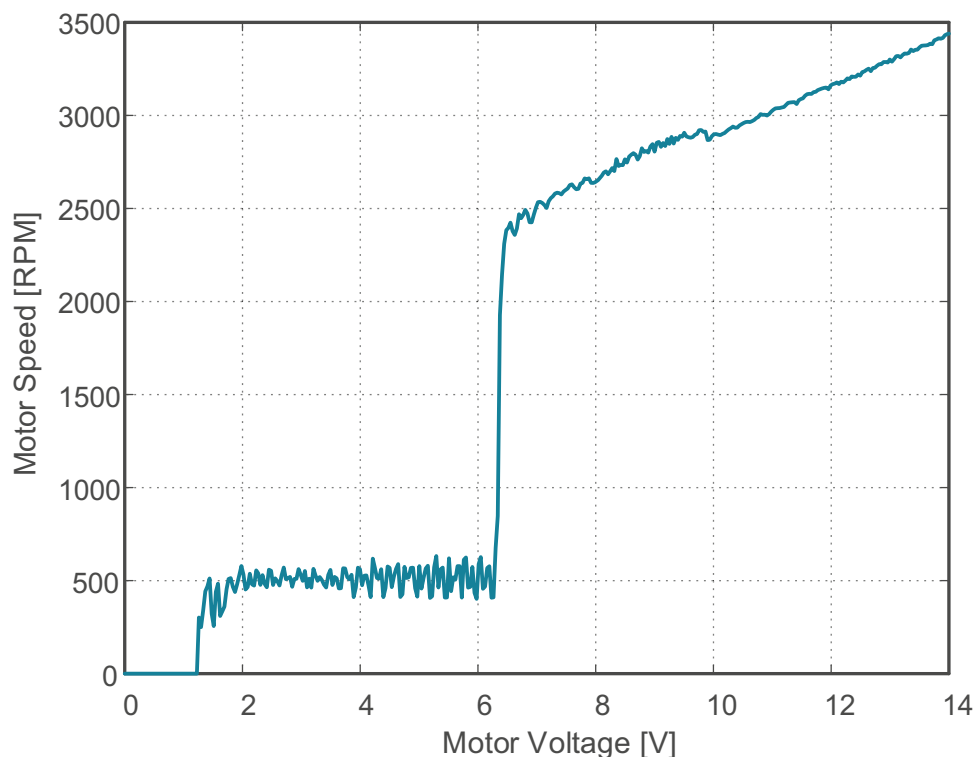
Source: Self-Authorship

Figure 37 shows the system considering the implementation of the SMA actuator and the ON/OFF control.

Figure 37 - Behavior of the System with SMA
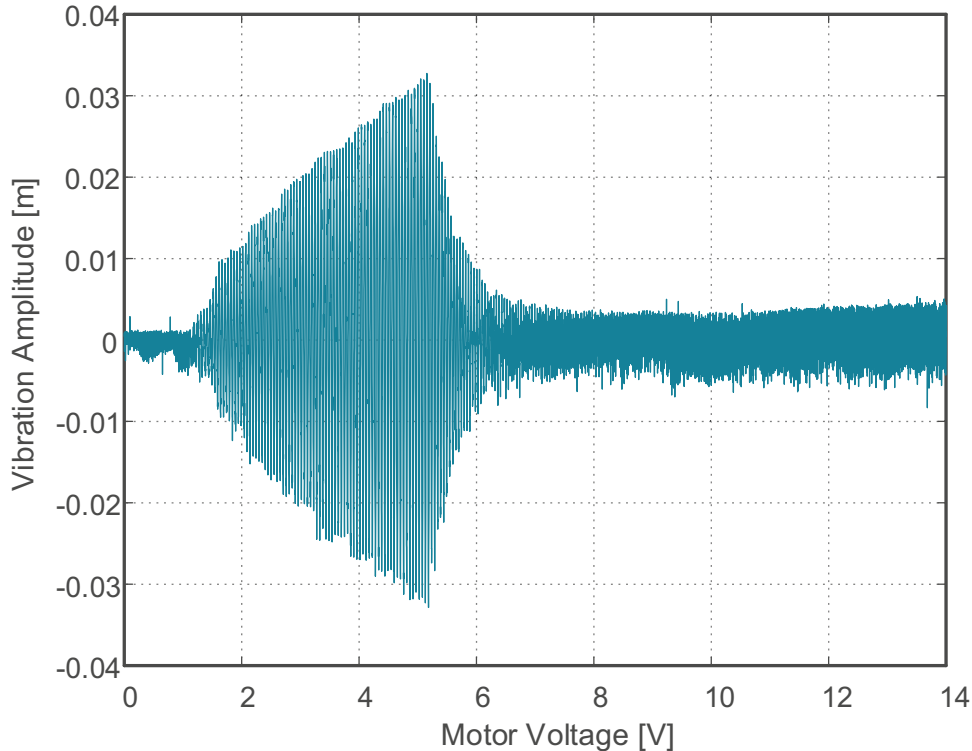
Source: Self-Authorship

The first observed change, when compared to the system without the actuator, is the reduction of the occurrence voltage of the jump effect. Where the Sommerfeld effect occurred approximately in 5.2 volts. This behavior also causes an advance of the jump effect, thus reducing the vibration amplitudes.

Figure 38 presents the current in the electric motor during the test with the SMA actuator and through that result is possible to see that there was a reduction in the current consumed by the motor during the jump effect, this reduction being approximate of 0.2 amperes when compared to the results without the SMA actuator.

Figure 39 presents the behavior of the motor speed during the test with the actuator implemented. Where it is possible to observe that there was a shorter period where the voltage applied to the motor did not correlate with an increase of its rotation, it is also possible to see less variation of the rotation values in this region when compared to the previously showed results for the system without the actuator.

Figure 38 - Electric Current during the Test with SMA
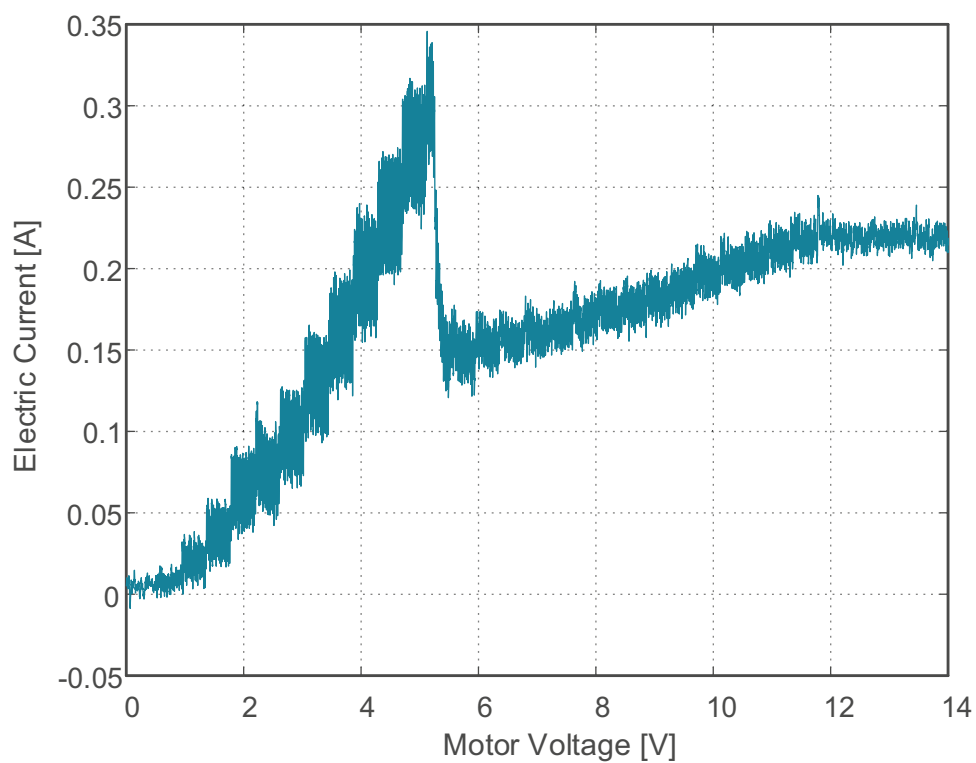
Source: Self-Authorship

Figure 39 - Motor Speed during the Sommerfeld Effect with the SMA
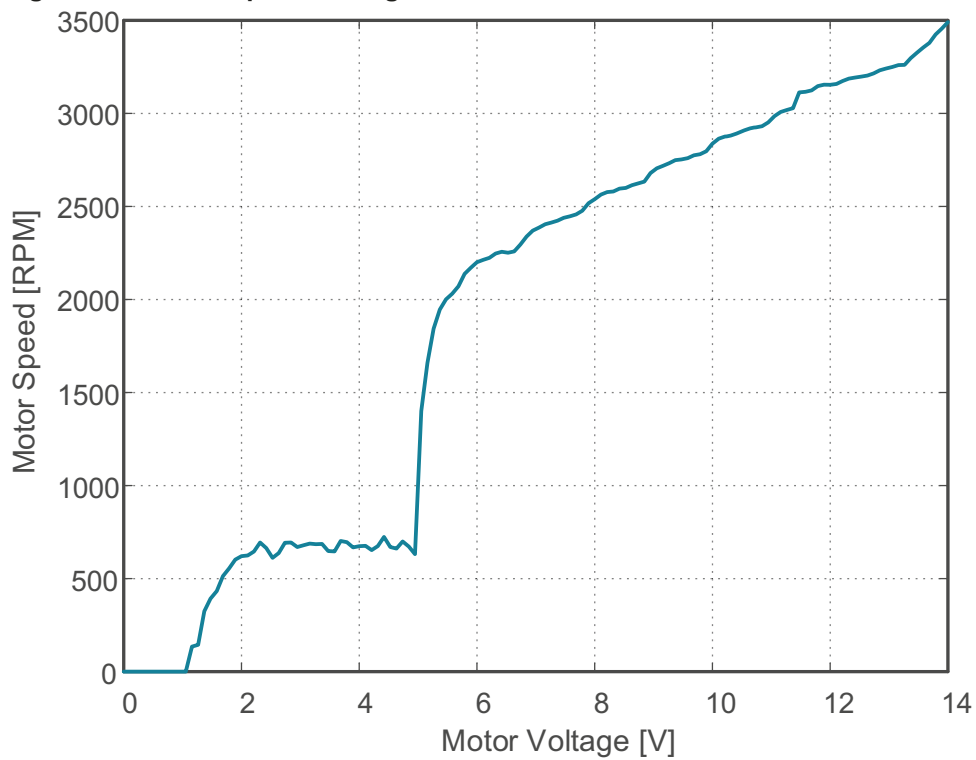
Source: Self-Authorship

Figure 40 shows the actuator signal, this being the current consumed by the SMA material. This figure also shows the moment that the controller acts in the system. As can be seen, a peak current of 1.1 amperes is consumed by the system.

Through the results presented in chapter 3, it is possible to observe that a value of 1.1 amperes in the actuator is able to fully transform the detwined martensite structure into the austenite form, and consequently allows full recovery of the actuator. The graphic of the current applied in the actuator also shows the little actuation time needed, where basically the system shuts down when the angular frequency shows a low value. Also, it is possible to see a great oscillation in the current during the actuation. This is caused by the vibration of the structure, where the SMA wire is stretched and relieved as the system moves thus, changing his section area and consequently the electrical resistance of the material.

Figure 40 - Control Signal
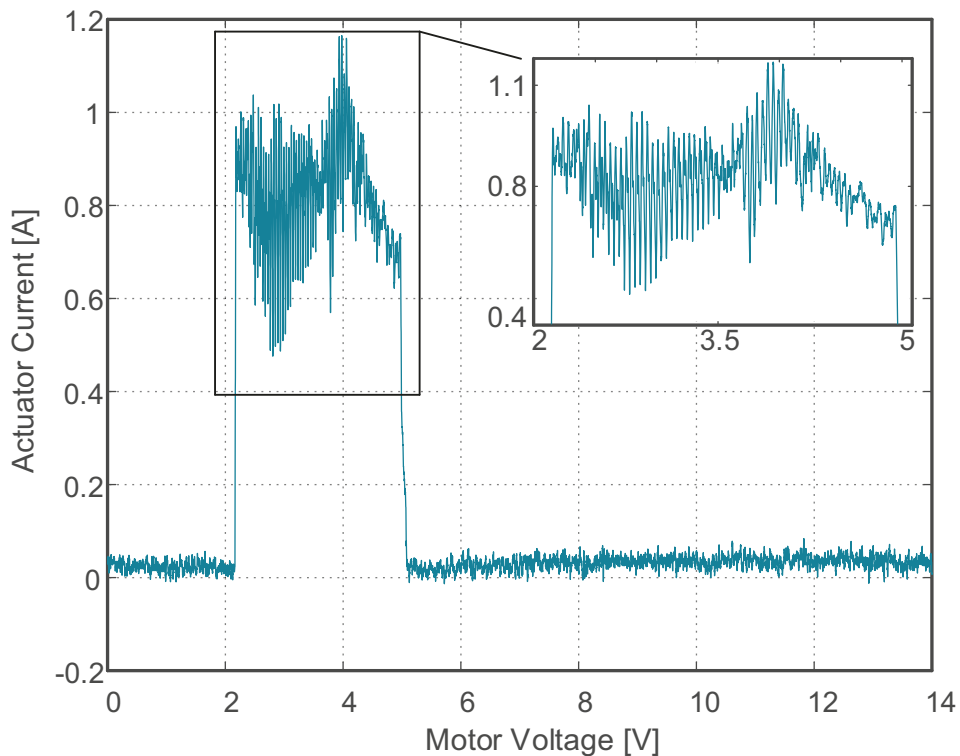
Figure 41 shows the comparison between the results for the vibration behavior without the actuator and with the SMA actuator (Figure 34 and 37, respectively).

With these results, some comments on the proposed controller functionality can be formulated. Considering that the control is activated only after a certain

moment by the controller (when the frequency of the system is near to the jump frequency), it is not possible to perceive a sudden change of the system initial response, where it is noticed that the initial amplitudes are very similar, only changing the voltage where the jump occurs. This show how strong is the dependence of the non-ideal system with its initial conditions. After the controller starts, the SMA material contracts through the passage of the electric current, thus making a force on the mechanical structure.

Through the final results, it is also possible to observe that the proposed control was able to reduce the peak of vibration amplitude by 42.59%, also causing the jump to occur almost 2 volts before the uncontrolled system. This is a very good result, meaning the reduction of the energy spent by the electromechanical system, and less physical wear due to the lower amplitudes of vibration.

Figure 41 - Comparison of the System with the SMA and Control
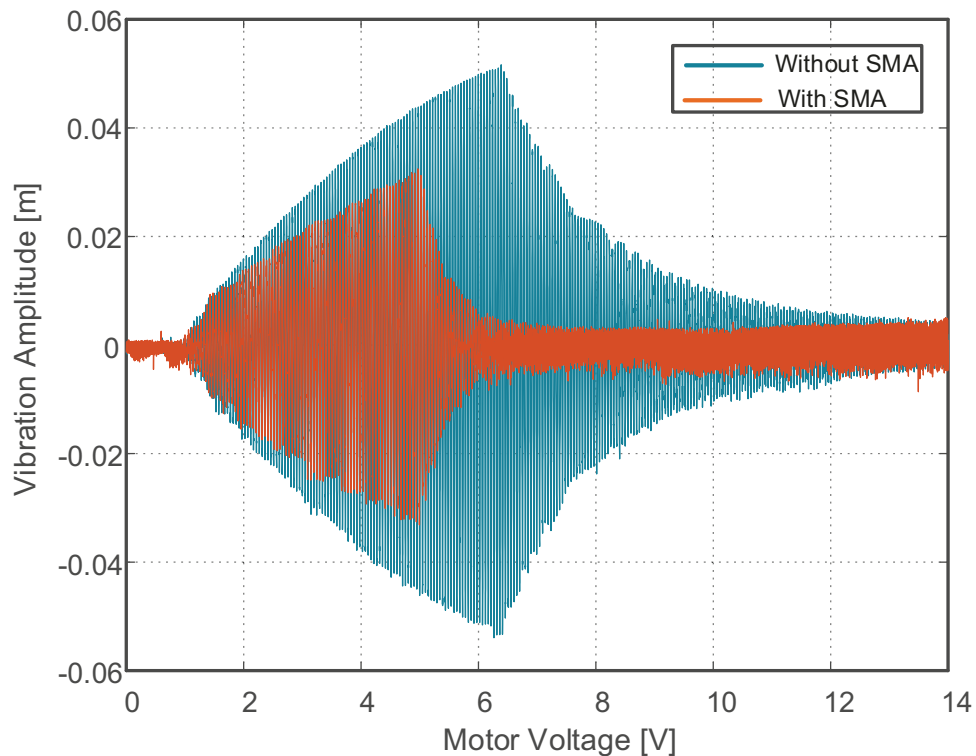
Source: Self-Authorship

5.3 SUMMARY

The experimental investigation of the non-ideal system coupled with the SMA actuator was made through the construction of a prototype. The system was built and instrumented.

This chapter proposed the attenuation and control of the non-ideal behavior and vibration through the use of an SMA actuator. The actuator has a form of a wire mechanically attached to the system. This SMA material is installed with a specific pre-load. When activated, the actuator contracts physically, generating a mechanical force that increases the stiffness of the system, reducing the vibration amplitudes of the system and removing it from the Sommerfeld effect region.

The results experimentally obtained for the non-ideal system without the SMA actuator show great similarity with the results of the non-ideal system mathematically modeled in chapter 4. This shows that the parameters obtained are very capable to represent the real system.

It is important to notice the influence of the non-ideal behavior both in the voltage and electric current consumed by the system, where the system shows peaks on consume near the resonance region. The experimental results of the proposed ON/OFF control with the shape memory alloy actuator showed a good ability to reduce the Sommerfeld effect and the amplitudes of vibration, and due to the advance of the jump occurrence, the voltage peaks and electric current were also reduced.

6 CONCLUSIONS, CONTRIBUTIONS AND FUTURE WORKS

This chapter presents the conclusions, main contributions of this thesis and some future work recommendations regarding the use of the SMA actuators for vibration attenuation in a non-ideal system.

6.1 CONCLUSIONS

Chapter 2

This chapter reviews the fundamentals of smart materials giving emphasis to shape memory alloys, i.e., a group of metallic alloys that are able to return to a predefined shape after being plastically deformed by increasing their temperature. In this chapter are discussed advantages, the most common applications, and their most important mathematical models.

Several phenomenological mathematical models attempting to reproduce the behavior of an SMA actuator have been created. Tanaka's model was the first to emerge. In this model, three interdependent state variables are considered to define the behavior of the SMA material. This model was well received, and other adapted versions of this model were further developed. The Liang model changed the exponential martensitic fraction equations by equations as functions of cosine and later, Brinson divided into two the portions of the martensitic fraction: one originating from the stress and another from the temperature. Elahinia proposed a new model that is better suited to experimental situations. Even though there are several phenomenological models, it is perceived that they are very similar in concept. All models use the same constitutive equation for the SMA,

Chapter 3

In this chapter, a system for the characterization of an SMA actuator was built. The structure was described and the procedures for data acquisition were defined. The behavior of an SMA actuator was experimentally studied, where it was analyzed for its displacement, the temperatures and the electric current consumed for fixed values of electric voltage. Is also studied a method to obtain the heat transfer parameter using experimentally obtained surface temperatures of the actuator.

Through the results obtained, it was possible to observe the evolution of the temperature in an SMA material when an electric voltage is applied. The material showed an almost linear correlation between the voltage applied and the surface temperature. However, the deformation recovery of the SMA material requires a specific temperature to fully occur, this being the A_f point, where values of temperature below A_f only serve to partially recover the deformation of the material.

It was also possible to observe the linear behavior of the experimental convection parameter which occurs in the material during the heating and cooling process. The values of the convention component were used to simulate the temperature profiles suffered by the material during the heating caused by the Joule effect and the natural cooling of the material, where the results showed a good correlation with the real behavior. This heat transfer model allied with the obtained parameters can then be used to obtain the temperatures values of the material in different future applications.

Chapter 4

This chapter focuses on the non-ideal type systems. Initially, the non-ideal systems are defined, with emphasis on the Sommerfeld effect, i.e., a special effect that causes the loss of energy applied in the system. Furthermore, a non-ideal system composed of a beam and an unbalanced DC motor was described, mathematically modeled and numerically simulated. All the numerical simulations were performed with the aid of a Runje-Kutta algorithm, being used experimentally obtained parameters.

The mathematical model was obtained through the use of the Lagrange's equations. For the electric motor, it was decided to use the complete set of equations that represent this type of system. This allowed a better relationship of the simulated system with the actual system. The results of the numerical simulations for the system were able to represent the expected non-ideal effects. The Sommerfeld effect was clearly shown in the results, where graphs for the voltage of occurrence of the effect were also possible to acquire. This showed that the system of equations, as well as the coupling of the mechanical part with the electrical part, was sufficient to demonstrate the non-ideal behavior. The jump was shown to occur at a low electrical voltage. This was due to the high nominal speed of the chosen motor. Since the

mechanical system has a low natural frequency, a low motor speed is enough to cause system instability.

Chapter 5

In this chapter, the experimental part of the non-ideal system was projected and built. The instrumentation used to capture the vibration signals of the system was fully described. All the data was captured through a program written in the Labview® using a CompacRIO Controller. It has proposed the installation of an SMA actuator with the objective of reducing the vibration and the Sommerfeld effect present in the non- ideal system.

The proposed control has the objective to actuate in the system when the frequency of the system is reaching some high and unstable value. When the control is switched on, the SMA material is activated, executing a force on the mechanical structure.

The jump graphs considering the frequency of the motor and considering the applied voltage show the loss of energy in the system, especially when it arrives near the resonance region.

The controller has shown a great performance reducing almost 50% of the vibration peak, also significantly reducing the Sommerfeld effect.

6.2 MAIN CONTRIBUTION

A set of experimental parameters for a shape memory alloy actuator heat transfer model:

Both the methodology described and the parameters obtained for an SMA type actuator can be used for future numerical simulations and various other applications. Since the parameters come from an actuator that already exists, this facilitates the correlation of future numerical simulations with the expected results obtained in a real situation.

A method of reducing the Sommerfeld effect present in a non-ideal system:

The proposal of an actuator for attenuation of the Sommerfeld effect (jump phenomenon) was shown. The control method proposed has the advantage of low

energy cost when compared to an always-on system. This methodology can be extended to other types of non-ideal systems, where possibly good results can also be obtained.

A set of experimental parameters for a non-ideal system:

Both the methodology described and the parameters obtained for the non-ideal system can be used for future numerical simulations and various other applications.

6.3 RECOMMENDATIONS FOR FUTURE WORKS

Experimental tests on others non-ideal systems:

Due to a large number of types of systems that may exhibit some kind of non-ideal behavior, there are several possibilities in numerical and experimental research on this subject. Studies can be done considering new types of systems, with more than one non-ideal source or with others types of coupling. Research can also be done considering new types of controllers, actuators and new ways of harnessing energy from non-ideal systems (energy harvesting).

Study other types of smart materials and applications in non-ideal systems:

The SMA type actuators had shown themselves as a quite promising option in some vibration control applications. However, as these actuators have a limited frequency range of performance, other options of smart materials or even the combination of the SMA with others smart materials is also a very promising option in future studies which consider systems with higher frequencies of actuation. In this new approach, the limitations of one material could be supplied by another actuator, forming a more complex and robust system.

REFERENCES

BALTHAZAR, J. M. et al. An overview on non-ideal vibrations. **Meccanica**, v. 38, n. 6, p. 613–621, 2003.

BALTHAZAR, J. M. et al. A review of new vibration issues due to non-ideal energy sources. **Dynamical Systems and Control**, p. 237–258, 2004.

BRINSON, L. C. One-dimensional constitutive behavior of shape memory alloys: thermomechanical derivation with non-constant material functions and redefined martensite internal variable. **Journal of intelligent material systems and structures**, v. 4, n. 2, p. 229–242, 1993.

CENGEL, Y. A.; GHAJAR, A. J.; KANOGLU, M. **Heat and mass transfer: fundamentals & applications**. [s.l.] McGraw-Hill New York, 2011. v. 4

ELAHINIA, M. H. **Effect of system dynamics on shape memory alloy behavior and control.** Dissertation—[s.l: s.n.].

ELAHINIA, M. H.; ASHRAFIUON, H. Nonlinear control of a shape memory alloy actuated manipulator. **Journal of vibration and acoustics**, v. 124, n. 4, p. 566–575, 2002.

FENILI, A. **Modelagem matemática e análise dos comportamentos ideal e não ideal de estruturas flexíveis de rastreamento**. Phd. Dissertation—Unicamp: [s.n.].

GORI, F.; SERRANO, M.; WANG, Y. Natural convection along a vertical thin cylinder with uniform and constant wall heat flux. **International journal of thermophysics**, v. 27, n. 5, p. 1527–1538, 2006.

KONONENKO, V. O. **Vibrating systems with a limited power supply**. [s.l.] Iliffe, 1969.

LAGOUDAS, D. C. **Shape memory alloys: modeling and engineering applications**. [s.l.] Springer Science & Business Media, 2008.

LEO, D. J. **Engineering analysis of smart material systems**. [s.l.] John Wiley & Sons, 2007.

LIANG, C.; ROGERS, C. A. One-dimensional thermomechanical constitutive relations for shape memory materials. **Journal of intelligent material systems and structures**, v. 8, n. 4, p. 285–302, 1997.

MACHADO, L.; SAVI, M. Medical applications of shape memory alloys. **Brazilian journal of medical and biological research**, v. 36, n. 6, p. 683–691, 2003.

MAVROIDIS, C. Development of advanced actuators using shape memory alloys and electrorheological fluids. **Research in Nondestructive Evaluation**, v. 14, n. 1, p. 1–32, 2002.

PAIVA, A.; SAVI, M. A. An overview of constitutive models for shape memory alloys. **Mathematical problems in engineering**, v. 2006, 2006.

PICCIRILLO, V.; TUSSET, A. M.; BALTHAZAR, J. M. Dynamical jump attenuation in a non-ideal system through a magnetorheological damper. **Journal of Theoretical and Applied Mechanics**, v. 52, n. 3, p. 595–604, 2014.

RAO, S. S.; YAP, F. F. **Mechanical vibrations**. [s.l.] Prentice Hall Upper Saddle River, 2011. v. 4

SAADAT, S. et al. An overview of vibration and seismic applications of NiTi shape memory alloy. **Smart materials and structures**, v. 11, n. 2, p. 218, 2002.

SHIGLEY, J. E. **Shigley's mechanical engineering design**. [s.l.] Tata McGraw-Hill Education, 2011.

SUN, L. et al. Stimulus-responsive shape memory materials: a review. **Materials & Design**, v. 33, p. 577–640, 2012.

TANAKA, K. A thermomechanical sketch of shape memory effect: one-dimensional tensile behavior. **Res. Mechanica**, v. 18, p. 251–263, 1986.

APPENDIX A - Mechanical System Parameters

This appendix describes the process used to obtain all the parameters for the mechanical part (cantilever beam) of the system.

The mechanical structure consists of a cantilever aluminum beam with a concentrated mass at its tip (DC motor). This system can be modeled as an equivalent mass-spring-damper system, as can be seen in Figure 42.

Figure 42 - 1 DOF System
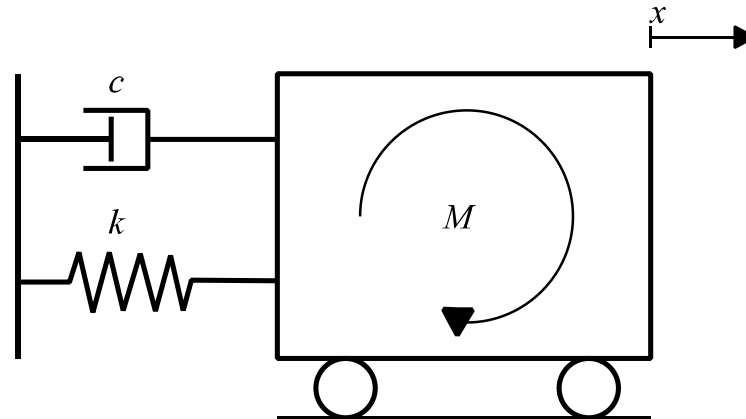
Source: Self-Authorship

This 1 DOF system can be represented by the Equation (A.1), where x is the displacement.

$$M\ddot{x} + c\dot{x} + kx = 0 \qquad (A.1)$$

To represent this system, three parameters are required: the stiffness constant (k), the mass of the system (M) and the viscous damping constant (c).

Stiffness Constant

The stiffness constant or spring constant is a type of massless link. In this type of system, a force occurs when the movement between two ends happens. This is the factor responsible for the elasticity of the structure (RAO, 2009). In this work the spring constant is considered linear and can be obtained by the Equation (A.2):

$$k = \frac{3EI}{l^3} \qquad (A.2)$$

where E is Young's modulus and I is the moment of inertia of the section, in this case, given by Equation (A.3).

$$I = \frac{bh^3}{12} \qquad (A.3)$$

Mass of the System

The mass is the element responsible for the inertia of the system and can be related to the natural frequency as shown in Equation (A.4).

$$f_n = \frac{1}{2\pi}\sqrt{\frac{k}{M}}$$

(A.4)

where f_n is the natural frequency, and M is the total mass of the system.

Viscous Damping Constant

Damping is the name given to the gradual reduction of the system vibration energy, also reducing its amplitudes (system response). This reduction occurs in practical systems due to the gradual conversion of the vibration energy into sound or heat. The damping of the system in this Master's Thesis is considered a viscous damping type. This type of damping occurs when a mechanical system vibrates in a fluidic environment (air, water, oil, etc.), being the damping force proportional to the velocity of the system, as shown in Equation (A.5) (RAO, 2009).

$$F_d = -c\dot{x}$$

(A.5)

To obtain this parameter was chosen to use the logarithmic decrement method. This experimental method uses the drop in time of the vibrations amplitudes of the free vibration to obtain a rate of variation of this parameter. When a system is excited by an external impulse, its response shows some kind of decay in time, which occurs naturally if the excitation force is removed. Through this decay, one can find the damping constant of the system.

The rate of change is given by the following equation.

$$\delta = \frac{1}{n}\ln\left(\frac{x_1}{x_2}\right)$$

(A.6)

where x_1 and xx_2 are the two amplitudes of vibration and n is the value of how many peaks separate the values of x_1 and x_2.

The Next step is to find the dimensionless damping factor, which is given by Equation (A.7).

$$\varsigma = \frac{\delta}{\sqrt{(2\pi)^2 + \delta^2}}$$

(A.7)

The critical damping is given by equation (A.8).

$$c_c = 2m\sqrt{\frac{k}{M}} \qquad \text{(A.8)}$$

As the damping factor for any vibration system is given by the ratio of the damping constant with the critical damping constant, this relation can be used to finally find the value of the damping constant.

$$c = \varsigma c_c \qquad \text{(A.9)}$$

Mechanical System Simulation

With the parameters of the system, numerical simulations can be done to validate the parameters and the mechanical system model.

Table 5 - Properties of the Mechanical System

Parameter	Value	Unit
M	0.190	kg
k	540.115	Pa
c	0.070	m

Source: Self-Authorship

Figure 43 presents a comparison between the behavior of the simulated system and the real system. The initial conditions used were: $x_1(0) = 0$, and $x_2(0) = 0$

There is a clear similarity between the two results, making the parameters obtained sufficient to describe the behavior of the mechanical system

Figure 43 - Comparison between the Real Mechanical System and his Simulation
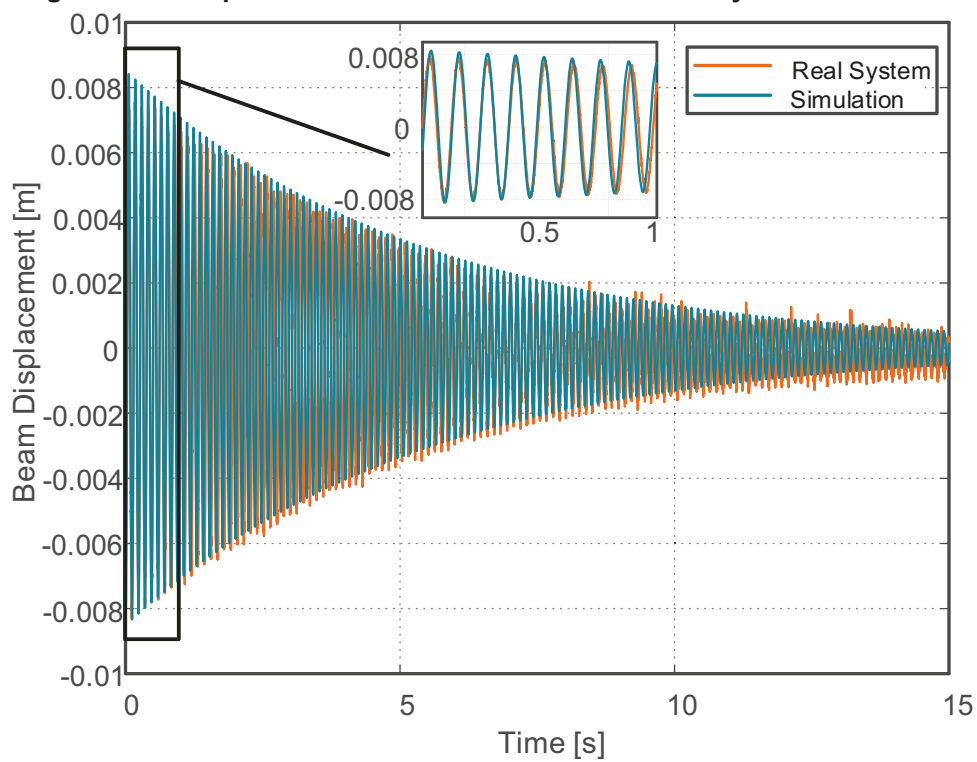
Source: Self-Authorship

APPENDIX B - Electric Motor Parameters

In this appendix are described the methods used to obtain the electric motor parameters. As seen in Chapter 4, two equations are required for the mathematical representation of the motor: Equation (3.8), for the mechanical part and Equation (3.9), for the electric part.

Electrical Resistance and Motor Armature Inductance

In order to obtain the inductance and electrical resistance values of the motor armature, it is possible to make direct measurements on the connections of the motor using the measuring instruments indicated for each parameter. Since the values found vary according to the angular position of the motor shaft, some measurements must be made by varying the motor angle until the smallest value is shown. This point then becomes the point for all the remaining measurements.

Torque Constant and Force Counter Against Electromotive

Considering equation (3.9) in steady state ($\frac{di_{mtr}}{dt} = 0$), we obtain Equation (B.1).

$$K_B = \frac{V_{mtr} - R_{mtr}i_{mtr}}{\dot{\varphi}}$$ (B.1)

The force constant against electromotive force was considered to be equal to the torque constant. According to Nise and da Silva (2002), these two constants have the same value when the system is fully adjusted.

Static Friction Constant

Making the assumptions of $\frac{d\dot{\varphi}}{dt} = 0$ and $\frac{di_{mtr}}{dt} = 0$, it is possible to rewrite the Equation in the form presented in the sequence.

$$b\varphi + F = K_T i_{mtr} = \tau$$ (B.2)

where τ is the torque generated by the motor.

Performing an energy balance in the electric motor and isolating the term relative to the mechanical losses, one obtains the Equation (B.3).

$$\tau = \left(\frac{V_{mtr} - R_{mtr}i_{mtr}}{\dot{\varphi}}\right)i_{mtr}$$ (B.3)

Figure 44 shows the graph that relates the angular frequency to the torque generated by the motor.

Figure 44 - The Relation between the Torque and the Angular Frequency
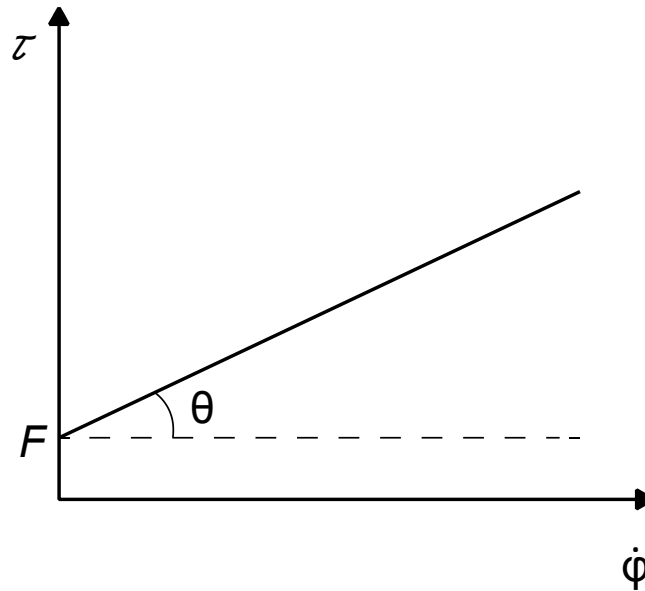
Analyzing the Figure 44 it's possible to obtain the static friction constant, that can be given by Equation (B.4).

$$b = \tan(\theta) \tag{B.4}$$

where θ is the angle formed between the graph F and the x-axis.

Inertia of the Motor

The inertia of the motor is given by equation (B.5).

$$J = b\dot{\varphi}_{ste} \tag{B.5}$$

where $\dot{\varphi}_{ste}$ is the steady-state speed multiplied by the value of time needed for the system to reach 38.6% of its steady-state speed.
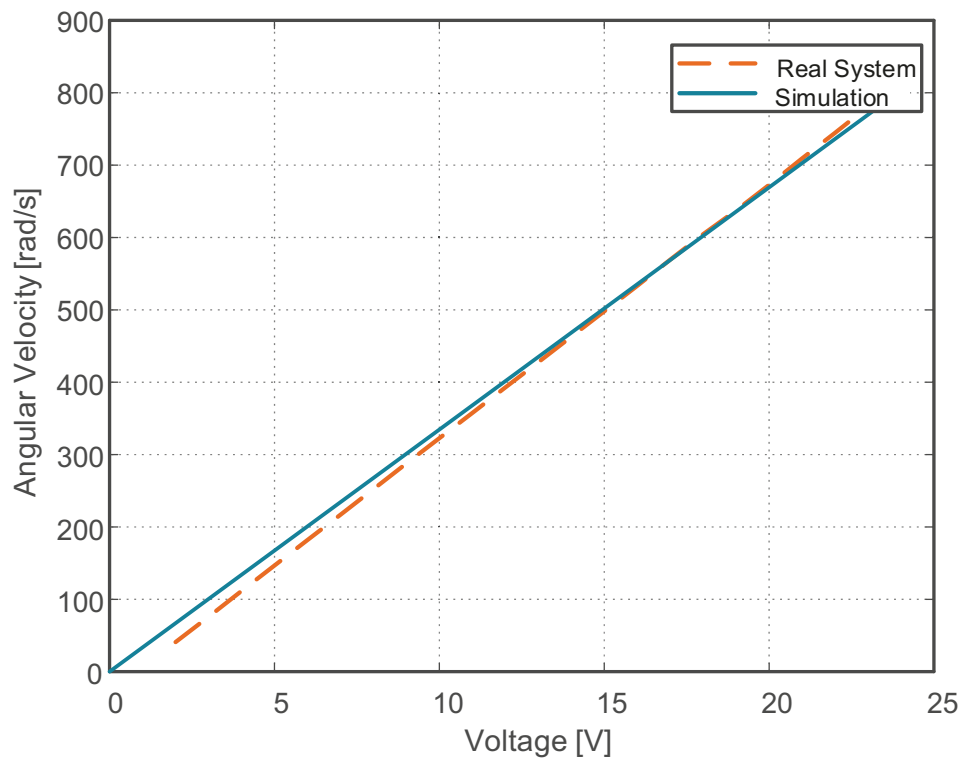
Electric Motor Simulation

Table 6 - Properties of the Electric Motor

Parameter	Value	Unit
R	41	Ω
L	$3.1x10^{-3}$	H
K_T	0.02114	$V.s \, / \, rad$
K_B	0.02114	$N.m \, / \, A$
b	$8.167x10^{-7}$	$N.m.s \, / \, rad$
J	$0.82x10^{-4}$	$kg.m^2$

Source: Self-Authorship

Figure 45 - Comparison between the Real Motor System and his Simulation

Source: Self-Authorship

APPENDIX C - Published Articles

During the studies in the Master's Degree course, the author published some articles with his supervisor and co-authors that are listed in the sequence.

1) Published articles in national and international journals

KOSSOSKI, ADRIANO; TUSSET, ANGELO M.; JANZEN, FREDERIC C.; ROCHA, RODRIGO T.; BALTHAZAR, JOSE M. ; BRASIL, REYOLANDO M.L.R.F.; NABARRETE, AIRTON. Jump Attenuation in a Non-Ideal System Using Shape Memory Element. MATEC WEB OF CONFERENCES, v. 148, p. 03003-4, 2018.

KOSSOSKI, A.; PICCIRILLO, V.; JANZEN, F. C.; BALTHAZAR, J. M.; TUSSET, A. M. Jump phenomenon in a nonideal system with shape memory element. REVISTA INTERDISCIPLINAR DE PESQUISA EM ENGENHARIA, v. 2, p. 156-173, 2016.

2) Published articles in national and international refereeing conferences

KOSSOSKI, A.; TUSSET, A. M.; SANTOS, G.; ROCHA, R. T.; JANZEN, F. C.; LENZ, W. B.; BALTHAZAR, J. M. Numerical and experimental analysis of a non-ideal type system. In: Congresso Nacional de Engenharia Mecânica, 2018, Salvador - Bahia. CONEM 2016, 2018.

LENZ, W. B.; TUSSET, A. M.; ROCHA, R. T.; JANZEN, F. C.; **KOSSOSKI, A.**; BALTHAZAR, J. M. Genetic algorithm optimization for horizontal axis wind turbine. In: Congresso Nacional de Engenharia Mecânica, 2018, Salvador - Bahia. CONEM 2018, 2018.

KOSSOSKI, ADRIANO; MARCELO TUSSET, ANGELO; SANTOS, GERSON; TUMOLIN ROCHA, RODRIGO; JANZEN, FREDERIC CONRAD; BALTHAZAR, JOSÉ MANOEL; Sommerfeld Effect in a Cantilever Beam with Double Non-ideal Sources. In: 24th ABCM International Congress of Mechanical Engineering, 2017, Curitiba. Proceedings of the 24th ABCM International Congress of Mechanical Engineering, 2017.

3) Book chapter published in an international book

LENZ, W. B.; TUSSET, A. M.; ROCHA, R. T.; JANZEN, F. C.; **KOSSOSKI, A.**; BALTHAZAR, J. M.; NABARRETE, A. The influence of anti-roll bar in the dynamics of full-car control. In: JAN AWREJCEWICZ; MAREK KAŹMIERCZAK; JERZY MROZOWSKI; PAWEŁ OLEJNIK. (Org.). Vibration, Control, and Stability of Dynamical Systems. 1ed.Łódź: ARSA Druk, 2017, v. 1, p. 279-290.